



# Direct numerical simulation and statistical analysis of stress-driven turbulent Couette flow with a free-slip boundary

Cite as: Phys. Fluids **31**, 085113 (2019); <https://doi.org/10.1063/1.5099650>

Submitted: 11 April 2019 . Accepted: 30 July 2019 . Published Online: 20 August 2019

Meng Li , and Di Yang 



View Online



Export Citation



CrossMark

## ARTICLES YOU MAY BE INTERESTED IN

[Wall turbulence response to surface cooling and formation of strongly stable stratified boundary layers](#)

Physics of Fluids **31**, 085114 (2019); <https://doi.org/10.1063/1.5109797>

[Artificial neural network mixed model for large eddy simulation of compressible isotropic turbulence](#)

Physics of Fluids **31**, 085112 (2019); <https://doi.org/10.1063/1.5110788>

[Effects of bulk viscosity on compressible homogeneous turbulence](#)

Physics of Fluids **31**, 085115 (2019); <https://doi.org/10.1063/1.5111062>

Scilight

Highlights of the best new research  
in the physical sciences

LEARN MORE!



# Direct numerical simulation and statistical analysis of stress-driven turbulent Couette flow with a free-slip boundary

Cite as: Phys. Fluids 31, 085113 (2019); doi: 10.1063/1.5099650

Submitted: 11 April 2019 • Accepted: 30 July 2019 •

Published Online: 20 August 2019



View Online



Export Citation



CrossMark

Meng Li  and Di Yang<sup>a)</sup> 

## AFFILIATIONS

Department of Mechanical Engineering, University of Houston, Houston, Texas 77004, USA

<sup>a)</sup>Electronic mail: [diyang@uh.edu](mailto:diyang@uh.edu).

## ABSTRACT

The effects of free-slip boundary on shear turbulence are studied numerically using the direct numerical simulation (DNS) approach. The flow considered in this study is a stress-driven turbulent Couette flow between two flat boundaries. The top boundary has an imposed shear stress in the streamwise direction and a free-slip condition for the streamwise velocity fluctuation and the spanwise velocity, and the bottom boundary satisfies the no-slip condition. This type of flow has a mean flow pattern similar to the turbulent plane Couette flow between a stationary flat plate and a moving flat plate but exhibits considerable differences in turbulence statistics due to the effects of the free-slip boundary. Statistical analysis based on the DNS data and theoretical derivation based on Taylor series expansion show that near the free-slip surface the turbulence variances of the three velocity components vary as quadratic functions of the vertical distance from the boundary while the Reynolds shear stress exhibits a linear behavior, which are very different from the counterparts near the no-slip boundary. The free-slip surface condition also leads to zero horizontal vorticities at the surface but allows nonzero vertical vorticity in the meantime, leading to considerable differences in the near-boundary statistics of vorticities and coherent vortex structures. Comparison of three DNS runs with different grid resolutions shows that smoothly resolving the more energetic turbulent flow structures near the free-slip boundary requires a higher horizontal grid resolution than that used for resolving the structures near the no-slip boundary.

Published under license by AIP Publishing. <https://doi.org/10.1063/1.5099650>

## I. INTRODUCTION

Turbulent flows driven by surface shear stress occur commonly in the upper layer of oceans and lakes under surface wind stress forcing.<sup>1</sup> To model such types of flows, many prior studies have considered an idealized flow problem configuration, in which a mean shear stress is imposed on a rigid impermeable flat surface to drive the shear turbulence underneath and the turbulent fluctuation velocity is allowed to slip freely at the surface.<sup>2–4</sup> Similar to the turbulent flows over solid boundaries where the wall friction helps to maintain the velocity shear for turbulence generation, the mean shear stress acting on a free-slip surface generates a mean velocity gradient that produces turbulence via shear instability.<sup>5,6</sup> However, unlike the no-slip velocity condition on a solid surface where velocities are restricted to be zero at the boundary, on a free-slip surface the fluctuating velocity in the tangential directions of the surface

can have considerable spatial and temporal variations due to turbulence. Consequently, the characteristics of the turbulence near a free-slip boundary can be quite different from those near a no-slip boundary.<sup>7–10</sup>

In the past several decades, the characteristics of turbulent flows over no-slip boundaries have been studied extensively based on turbulent channel flows and Couette flows between two flat plates.<sup>11–20</sup> In contrast, shear-driven turbulent flows near free-slip surfaces have received less attention and the knowledge on their characteristics is less developed compared to those for the no-slip boundary cases. Many previous studies for the effects of free-slip boundaries on turbulent flows have focused on the pure “free surface” scenario, in which there is no shear stress applied and the surface is completely free of tangential forcing. Because of the lack of mean shear, the turbulence is usually generated by a no-slip surface on the opposite boundary of the free-slip boundary (i.e., turbulent open-channel

flows)<sup>7,10,21,22</sup> or decay in time due to the lack of mean shear or external forcing to sustain the turbulence.<sup>9,23</sup> In some studies, the free surface also features deformations either prescribed or excited by the turbulence underneath it, and artificial external forcing is applied in the bulk flow region far away from the boundary to generate turbulence that advects to the boundary to interact with the free surface.<sup>24,25</sup> Many interesting flow phenomena and valuable physical insights were obtained from these studies to improve our understanding on the effect of the free-slip boundary on turbulence. However, in these pure free-surface cases, the turbulence generation region is separated from the free-slip boundary, making the dynamics of turbulence considerably different from the conditions with mean surface shear. To date, the characteristics of turbulent flows near rigid free-slip boundaries in the presence of surface shear remain not well understood.

In this study, we investigate the effects of a free-slip boundary on the characteristics of a shear turbulent flow by applying direct numerical simulation (DNS) to model the stress-driven turbulent Couette flow. In particular, the flow is bounded by a no-slip impermeable flat surface at the bottom and a free-slip impermeable flat surface at the top, with periodic conditions on the lateral boundaries. A constant mean shear stress is applied in the streamwise direction at the top surface to drive the flow. This flow has a mean velocity profile similar to the classical turbulent plane Couette flow between a stationary bottom plate and a moving top plate.<sup>11,13,14,16</sup> At the top boundary, the imposed shear stress induces a constant vertical gradient of the mean streamwise velocity; the streamwise and spanwise velocity components are allowed to fluctuate on the top surface but have a zero vertical gradient for the fluctuating components. Such a type of stress-driven Couette flow has been employed as the base flow system for many prior numerical studies of turbulent flow over water waves.<sup>26–28</sup> By having a free-slip boundary and a no-slip boundary in a single flow system, the current flow configuration allows us to study the effects of free-slip boundary on the characteristics of shear turbulence and compare them to the counterparts near a no-slip boundary.

In this study, the stress-driven Couette flow is simulated using DNS at a Reynolds number of 180 defined based on the friction velocity and half-domain height. This relatively low Reynolds number is chosen because the turbulence statistics in this Reynolds number regime have been well studied and there are many reported DNS and experimental data available for comparison.<sup>11–14,16</sup> Three different grid resolutions are considered to assess the effect of the free-slip boundary on the computational cost of DNS, among which the lowest resolution case has comparable grid resolutions to prior DNS studies and the other two cases have even higher resolutions. To characterize the effects of the free-slip boundary on the turbulent flow, systematic statistical analyses on the mean and fluctuating components of the velocity field are performed. In particular, the vertical profiles of the mean velocity, turbulence variances, and Reynolds shear stress in the top and bottom boundary regions are quantified in detail. The balances of turbulent kinetic energy (TKE) budgets are investigated for both the individual components in the three directions and their total. Vorticity statistics and coherent vortex structures are also analyzed using planar averaging and conditional averaging methods. Based on these statistics, the effects of the free-slip boundary on the shear turbulence are studied and compared to the classical no-slip boundary case.

It is worth mentioning that in applications related to upper ocean boundary layer flows,<sup>2–4</sup> additional effects due to the surface waves are commonly considered. A widely used flow configuration in these studies is to model the ocean surface as a free-slip rigid flat surface with imposed wind shear stress, which is similar to the top boundary configuration considered in this study. The averaged effect of the surface waves on the shear-driven turbulence is then modeled by including a vortex force acting on the flow field as a result of the interaction between the wave-induced Stokes drift and the shear current, which leads to the generation of Langmuir circulations.<sup>1,29,30</sup> In these studies of Langmuir circulations, the simpler case of pure shear-driven turbulence without the wave Stokes drift effect is often used as the baseline case for comparison purpose, but the characteristics of the shear-driven turbulence near the free-slip surface itself has not been studied systematically in great detail. The DNS study reported in this paper, despite the idealized simulation setup without the wave effect, may provide useful insights to help understand the general characteristics of shear turbulence near a free-slip boundary.

This paper is organized as follows. The problem definition and numerical method are discussed in Sec. II. The DNS results are presented in Sec. III, and the statistics of shear turbulence near the free-slip and no-slip boundaries are analyzed and compared. Finally, conclusions are summarized in Sec. IV.

## II. PROBLEM DESCRIPTION AND NUMERICAL METHOD

As illustrated in Fig. 1, in this study, we consider a Couette type turbulent flow in a rectangular prism shape domain. The Cartesian coordinate system used in DNS is defined as  $\mathbf{x} = x_i (i = 1, 2, 3) = (x, y, z)$ , where  $x$  is for the streamwise direction,  $y$  is for the spanwise direction, and  $z$  is for the vertical direction. The origin of the  $z$  coordinate is set to be at the bottom boundary of the simulation domain. The corresponding velocity vector is defined as  $\mathbf{u} = u_i (i = 1, 2, 3) = (u, v, w)$ , where  $u$ ,  $v$ , and  $w$  are the components in  $x$ -,  $y$ -, and  $z$ -directions, respectively.

Within the simulation domain, the turbulent flow is governed by the three-dimensional incompressible Navier–Stokes equations in conservative form

$$\nabla \cdot \mathbf{u} = 0, \quad (1)$$

$$\frac{\partial \mathbf{u}}{\partial t} + \nabla \cdot (\mathbf{u}\mathbf{u}) = -\frac{1}{\rho} \nabla p + \nu \nabla^2 \mathbf{u}, \quad (2)$$

where  $\rho$  is the fluid density,  $p$  is the dynamic pressure, and  $\nu$  is the kinematic viscosity. Equations (1) and (2) are discretized using a Fourier-series-based pseudospectral method on evenly spaced collocated grid points in the horizontal directions. The standard 2/3-rule is used for eliminating the aliasing error in the nonlinear terms associated with the pseudospectral method.<sup>31,32</sup> In the vertical direction, a second-order finite-difference method is used for discretization based on staggered vertical grid points for  $(u, v, p)$  and  $w$ . For time advancement, the current DNS model uses a fractional-step projection method involving a velocity prediction step and a pressure correction step.<sup>33</sup> In the prediction step, the momentum equations (2) for  $(u, v, w)$  are advanced in time based on a semiexplicit scheme, with the second-order Adams–Bashforth scheme for the nonlinear convective terms and the second-order Crank–Nicolson scheme

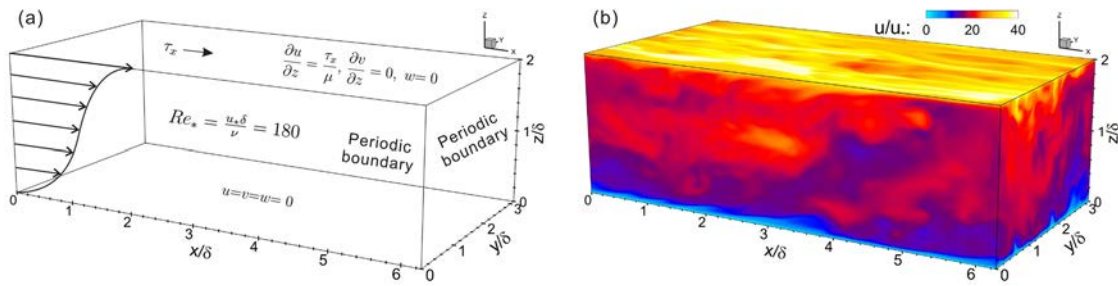


**FIG. 1.** Three-dimensional illustration of DNS of stress-driven turbulent Couette flow. The setup of the DNS is shown in (a), and a snapshot of the flow field obtained from the DNS is shown in (b), in which the contours of the instantaneous streamwise velocity (normalized by the friction velocity  $u_*$ ) are shown on the surfaces.

for the viscous diffusion terms. In the correction step, a Poisson equation for pressure is constructed based on the divergence-free condition in Eq. (1) and solved, and the resulting pressure field is used to project the predicted velocity into the divergence-free space to obtain the final velocity at the end of time advancement process for the current time step. More details for the numerical schemes and validations of the current DNS solver can be found in Ref. 34.

In this study, the DNS uses a computational domain of size  $(L_x, L_y, H) = (2\pi\delta, \pi\delta, 2\delta)$ , where  $L_x$  is the domain dimension in the  $x$ -direction,  $L_y$  is the domain dimension in the  $y$ -direction,  $H$  is the domain height in the  $z$ -direction, and  $\delta = H/2$  is the half-domain height. The flow satisfies the classical no-slip and impermeability conditions at the bottom boundary at  $z = 0$ , i.e.,

$$u = v = w = 0. \quad (3)$$

At the top boundary, the flow is not allowed to penetrate the flat boundary but can slip freely in the spanwise direction; the flow is driven by an imposed mean streamwise shear stress at the top boundary,  $\tau_x$ . The corresponding conditions at the top boundary are

$$\frac{\partial u}{\partial z} = \frac{\tau_x}{\mu}, \quad (4)$$

$$\frac{\partial v}{\partial z} = 0, \quad (5)$$

$$w = 0, \quad (6)$$

where  $\mu$  is the dynamic viscosity of the fluid. Let the time and horizontal average of a physical quantity  $f$  be denoted as  $\langle f \rangle$ , the corresponding turbulent fluctuation is  $f' = f - \langle f \rangle$ . Applying the time and horizontal average operator to the top boundary conditions gives  $\partial\langle u \rangle/\partial z = \tau_x/\mu$ ,  $\partial\langle v \rangle/\partial z = 0$ , and  $\langle w \rangle = 0$ . Thus, the velocity fluctuations at the top boundary satisfy the free-slip and impermeability conditions,  $\partial u'/\partial z = 0$ ,  $\partial v'/\partial z = 0$ , and  $w' = 0$ . With this configuration, the mean flow velocity profile is very similar to the turbulent plane Couette flow between a stationary bottom plate and a moving top plate, except that additional flow motions are allowed in the horizontal directions at the top boundary in the current flow configuration. This stress-driven Couette flow has also been used to study wind-wave interactions in many prior studies.<sup>26–28,35,36</sup>

We perform the DNS at a Reynolds number of  $Re_* = u_*\delta/\nu = 180$ , which is defined based on the turbulence friction velocity  $u_*$

and the half-domain height  $\delta$ . The friction velocity is related to the imposed shear stress as  $u_* = \sqrt{\tau_x/\rho}$ . This Reynolds number is chosen because the turbulent Couette flows and channel flows between two flat plates in this low Reynolds number regime have been well studied so that data are available for comparison to help study the differences in turbulent flow characteristics caused by the differences in the free-slip and no-slip boundary conditions. In this study, three DNS cases with identical simulation domain size and physical parameters but different numbers of computational grid points are considered, i.e., case R1 with  $384 \times 384 \times 193$  grid points, case R2 with  $192 \times 192 \times 193$  grid points, and case R3 with  $128 \times 128 \times 129$  grid points. The corresponding grid resolutions in wall units (i.e.,  $\Delta x^+$ ,  $\Delta y^+$ , and  $\Delta z^+$ , where the superscript “+” denotes normalization by the wall unit  $\nu/u_*$ ) are listed in Table I together with several other representative DNS runs from prior studies.<sup>12,14,16</sup> The vertical grid distribution is further discussed in the Appendix. Among these three cases considered in the current study, case R1 with the highest spatial resolution is the primary case, and its data are used for statistical analysis of the turbulent flow physics. The simulation was initialized with a divergence-free velocity field with random fluctuations and was run for 133 eddy turnover times,  $\tau_e = \delta/u_*$ , from which the statistics were obtained based on the last 10 eddy turnover times  $123 \leq t/\tau_e \leq 133$ . As shown in Table I, even the lowest resolution case R3 has comparable grid resolution as other prior DNS studies of turbulent channel flows or Couette flows. However, as will be discussed in Sec. III, the free-slip boundary conditions for the fluctuating velocity components  $u'$  and  $v'$  generate apparent differences for the turbulence statistics and coherent flow structures near the free-slip top boundary when compared to those near the no-slip bottom boundary. Consequently, the computational cost for resolving the essential turbulence flow phenomena near the free-slip boundary is significantly higher than that for the bottom no-slip boundary. The three different grid resolutions considered in this study are used to illustrate this increase of computational cost, as shown in Sec. III E.

Note that cases R1–R3 use a simulation domain of  $(2\pi\delta, \pi\delta, 2\delta)$ , which has smaller horizontal dimensions than those used in the previous studies listed in Table I. This smaller horizontal domain size allows us to achieve high grid resolutions in the  $x$ - and  $y$ -directions with affordable computational cost in the primary case R1. To check that the horizontal domain size is sufficient, an additional case R4 with a larger simulation domain of  $(4\pi\delta, 2\pi\delta, 2\delta)$  is also considered. For the streamwise velocity component  $u$ , the two-point spatial

TABLE I. Resolution used in DNS of turbulent Couette flows and channel flows.

Flow type	Reynolds number	Domain size	Grid number	Resolution in wall units		
	$Re_x = u_* \delta / \nu$	$(L_x, L_y, H)$	$N_x \times N_y \times N_z$	$\Delta x^+$	$\Delta y^+$	$\Delta z^+$
Channel flow <sup>12</sup>	180	$(4\pi\delta, 2\pi\delta, 2\delta)$	$192 \times 160 \times 129$	11.8	7.1	0.05–4.4
Couette flow <sup>14</sup>	157	$(4\pi\delta, 2\pi\delta, 2\delta)$	$128 \times 128 \times 65$	15.4	7.7	0.18–7.6
Couette flow <sup>16</sup>	130	$(4\pi\delta, 2\pi\delta, 2\delta)$	$144 \times 96 \times 96$	10.8	13.5	1.0–5.5
Couette flow (case R1)	180	$(2\pi\delta, \pi\delta, 2\delta)$	$384 \times 384 \times 193$	2.9	1.5	0.09–3.5
Couette flow (case R2)	180	$(2\pi\delta, \pi\delta, 2\delta)$	$192 \times 192 \times 193$	5.9	2.9	0.09–3.5
Couette flow (case R3)	180	$(2\pi\delta, \pi\delta, 2\delta)$	$128 \times 128 \times 129$	8.8	4.4	0.13–5.4
Couette flow (case R4)	180	$(4\pi\delta, 2\pi\delta, 2\delta)$	$256 \times 256 \times 129$	8.8	4.4	0.13–5.4

autocorrelations as a function of streamwise separation  $\xi$  and spanwise separation  $\psi$  are calculated according to Refs. 6, 12, 14, and 37,

$$R_{uu}(\xi, z) = \frac{\langle u'(x, y, z)u'(x + \xi, y, z) \rangle}{\langle u'(x, y, z)u'(x, y, z) \rangle}, \quad (7)$$

$$R_{uu}(\psi, z) = \frac{\langle u'(x, y, z)u'(x, y + \psi, z) \rangle}{\langle u'(x, y, z)u'(x, y, z) \rangle}, \quad (8)$$

where  $u'$  is the turbulent fluctuation of  $u$  and  $\langle \cdot \rangle$  denotes the time and horizontal average as defined earlier. The autocorrelations for the other two velocity components,  $R_{vv}$  and  $R_{ww}$ , are defined

similarly. Figure 2 compares the two-point spatial autocorrelations obtained from cases R1 and R4 using two different domain sizes and shows good agreement between the two cases. Note that in a turbulent Couette flow, the autocorrelation of the streamwise velocity,  $R_{uu}$ , does not approach zero with large streamwise spatial separation  $\xi$  even when using extreme large horizontal simulation domain sizes due to the existence of large coherent structures in the turbulent plane Couette flows.<sup>37</sup> Nevertheless, the results obtained from the current DNS cases are consistent with those reported in the literature for turbulent Couette flows.<sup>14,37</sup> We choose to use the domain size  $(2\pi\delta, \pi\delta, 2\delta)$  for the primary simulation case R1 in this study due to its lower computational cost for achieving higher grid resolutions.

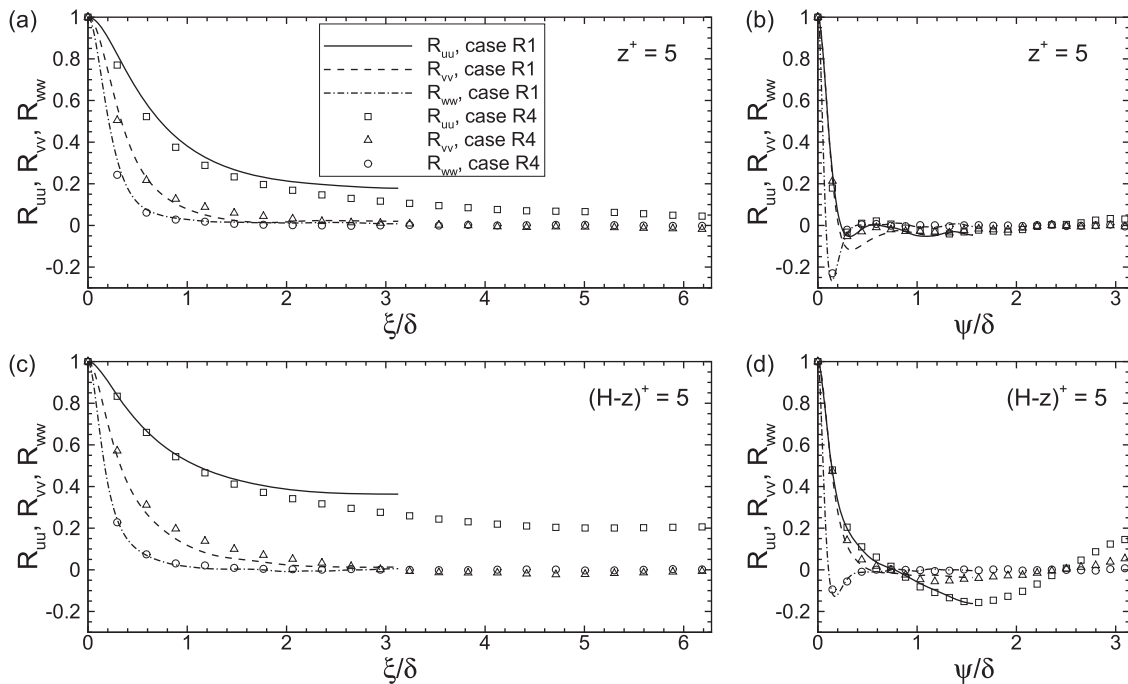


FIG. 2. Two-point spatial autocorrelations  $R_{uu}$ ,  $R_{vv}$ , and  $R_{ww}$  as a function of the [(a) and (c)] streamwise separation  $\xi/\delta$  and [(b) and (d)] spanwise separation  $\psi/\delta$ , at [(a) and (b)]  $z^+ = 5$  and [(c) and (d)]  $(H - z)^+ = 5$ . The results from case R1 with the  $(2\pi\delta, \pi\delta, \delta)$  domain size are indicated by lines, and those from case R4 with  $(4\pi\delta, 2\pi\delta, \delta)$  domain size are indicated by symbols.

### III. RESULTS

#### A. Statistics of mean and fluctuating velocities

Figure 3(a) shows the profile of the mean (i.e., time and horizontal average) streamwise velocity normalized by the friction velocity, i.e.,  $\langle u \rangle^+ = \langle u \rangle / u_*$ . When plotted in  $z/\delta$ , the mean velocity profile consists of two strong shear layers near the bottom and top boundaries and a constant-slope region in the center of the simulation domain, which is similar to the profile in the turbulent plane Couette flows between two no-slip flat plates.<sup>11,13,14,16,17</sup> The difference in the two boundary regions can be viewed by plotting the profile in each region using its own local distance from the boundary in wall units. Figure 3(b) shows the semilog plot for the profiles of  $\langle u \rangle^+$  as a function of  $z^+$  near the bottom boundary and  $(\langle u \rangle_{top} - \langle u \rangle)^+$  as a function of  $z_t^+ = (H - z)^+$  near the top boundary, where  $\langle u \rangle_{top} = \langle u \rangle(z = H)$ . Both profiles exhibit a linear profile in the viscous sublayer near the corresponding neighboring boundary and a logarithmic profile in the log-law region. In Fig. 3(b), one reference curve based on the linear profile  $\langle u \rangle^+ = z^+$  and two reference curves based on the standard log-law profiles  $\langle u \rangle^+ = (1/\kappa) \ln(z^+) + B$  and  $(\langle u \rangle_{top} - \langle u \rangle)^+ = (1/\kappa) \ln(z_t^+) + B$  are plotted for comparison. As shown in the figure, the mean velocity profile near the no-slip boundary follows the linear profile well up to  $z^+ \approx 5$ . Near the free-slip boundary, the linear profile region only extends to about  $z^+ \approx 2$ . The current DNS result shows that both the bottom and top boundary log-law profiles obey the standard log-law with the von Kármán constant  $\kappa = 0.41$ , but the values for the profile offset constant  $B$  differs for the two profiles. The mean velocity profile of the bottom layer shows good agreement with the reference log-law curve based on the classical value of  $B = 5.2$ ,<sup>6,11</sup> which is within the range of previously reported values of 4.5–6.0.<sup>14,16,37</sup> For the top boundary profile, a smaller offset constant of  $B = 2$  yields good agreement with the profile obtained from the current DNS.

Note that the top boundary layer profile is plotted based on  $(\langle u \rangle_{top} - \langle u \rangle)^+$ . The smaller offset constant  $B$  indicates that the mean streamwise velocity at a  $z_t^+$  in the log-law region of the top boundary layer differs less from its corresponding boundary value when compared to the counterpart at the same  $z^+$  near the bottom boundary. Although the physical mechanism for determining the

value of  $B$  remains an open question and previous studies suggested that  $B$  varies over a range even for solid-wall boundary layer turbulence,<sup>6,14,16,37</sup> in the current DNS the difference in  $B$  for the mean velocity profile near the no-slip and free-slip boundaries may be due to the more intensive turbulent motions and momentum mixing near the free-slip boundary. Figure 4 shows the contours of the velocity fluctuations ( $u'$ ,  $v'$ ,  $w'$ ) and the streamwise vorticity  $\omega_x$  on the two horizontal planes located at 5 wall units away from the bottom and top boundaries. Note that because the mean velocity components  $\langle v \rangle$  and  $\langle w \rangle$  are zero in the simulated Couette flow, the instantaneous spanwise and vertical velocity fluctuations satisfy  $v' = v$  and  $w' = w$ , respectively. As shown in Fig. 4, the horizontal flow fields near both boundaries exhibit long streaky structures for  $u'$ . The magnitudes and spatial patterns of  $v'$ ,  $w'$ , and  $\omega_x$  show apparent differences near the two boundaries, with the plane near the free-slip top boundary exhibiting more intensive turbulent fluctuations.

The higher contour magnitudes for  $u'$ ,  $v'$ , and  $w'$  on the plane at  $z/\delta = 1.97$  than those on the plane at  $z/\delta = 0.03$  suggest that the turbulent flow motions are more energetic in the region near the free-slip top boundary than those near the no-slip bottom boundary. This difference in the turbulent kinetic energy near the two boundaries can also be seen from the one-dimensional energy spectra. Figure 5 shows the streamwise and spanwise energy spectra for the three velocity components at  $z^+ = 5$  and  $(H - z)^+ = 5$ . The spectra at  $z^+ = 5$  near the bottom no-slip boundary obtained from the current DNS case R1 show good agreement with the spectra at similar location obtained from the DNS of turbulent channel flow from Ref. 12. Consistent with the more intensive turbulent fluctuations observed from Fig. 4, the spectra for all the three velocity components exhibit higher value at  $(H - z)^+ = 5$  near the free-slip boundary than those at  $z^+ = 5$  near the no-slip boundary.

The similarities and differences in turbulence statistics near the bottom and top boundaries can also be seen clearly from the profiles of Reynolds stress components in Fig. 6. Near both boundaries, the magnitudes of turbulence variances follow the order of  $\langle u'u' \rangle > \langle v'v' \rangle > \langle w'w' \rangle$ . When plotted based on the wall units, the turbulence variances obtained from the current DNS agree with the experimental data from the literature.<sup>11,13</sup> Note that all the three

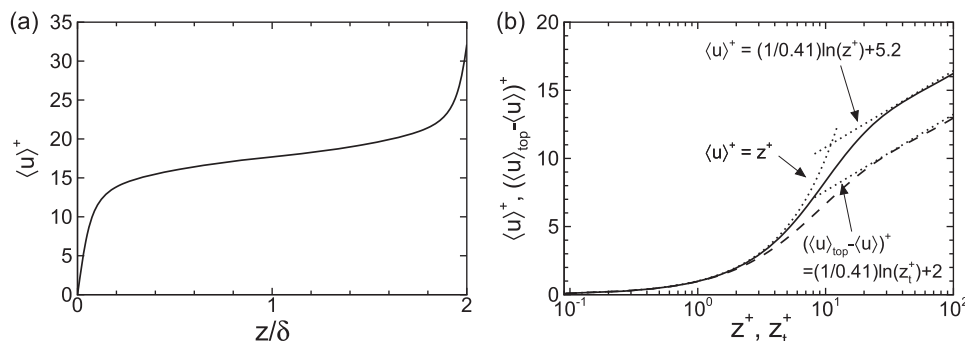


**FIG. 3.** Mean velocity profile in (a)  $z/\delta$  and (b) local wall units  $z^+$  and  $z_t^+ = (H - z)^+$ . In panel (b), the velocity profile near the bottom boundary is plotted based on  $\langle u \rangle^+$  and  $z^+$  (solid line), the velocity profile near the top boundary is plotted based on  $(\langle u \rangle_{top} - \langle u \rangle)^+$  and  $z_t^+$  (dashed line), and reference linear and logarithmic profiles are denoted by dotted lines. In the log-law regions near the no-slip bottom boundary and free-slip top boundary, the mean velocity profiles follow  $\langle u \rangle^+ = (1/\kappa) \ln(z^+) + B$  and  $(\langle u \rangle_{top} - \langle u \rangle)^+ = (1/\kappa) \ln(z_t^+) + B$ , respectively. For the no-slip boundary case,  $(\kappa, B) = (0.41, 5.2)$ ; for the free-slip boundary case,  $(\kappa, B) = (0.41, 2)$ .

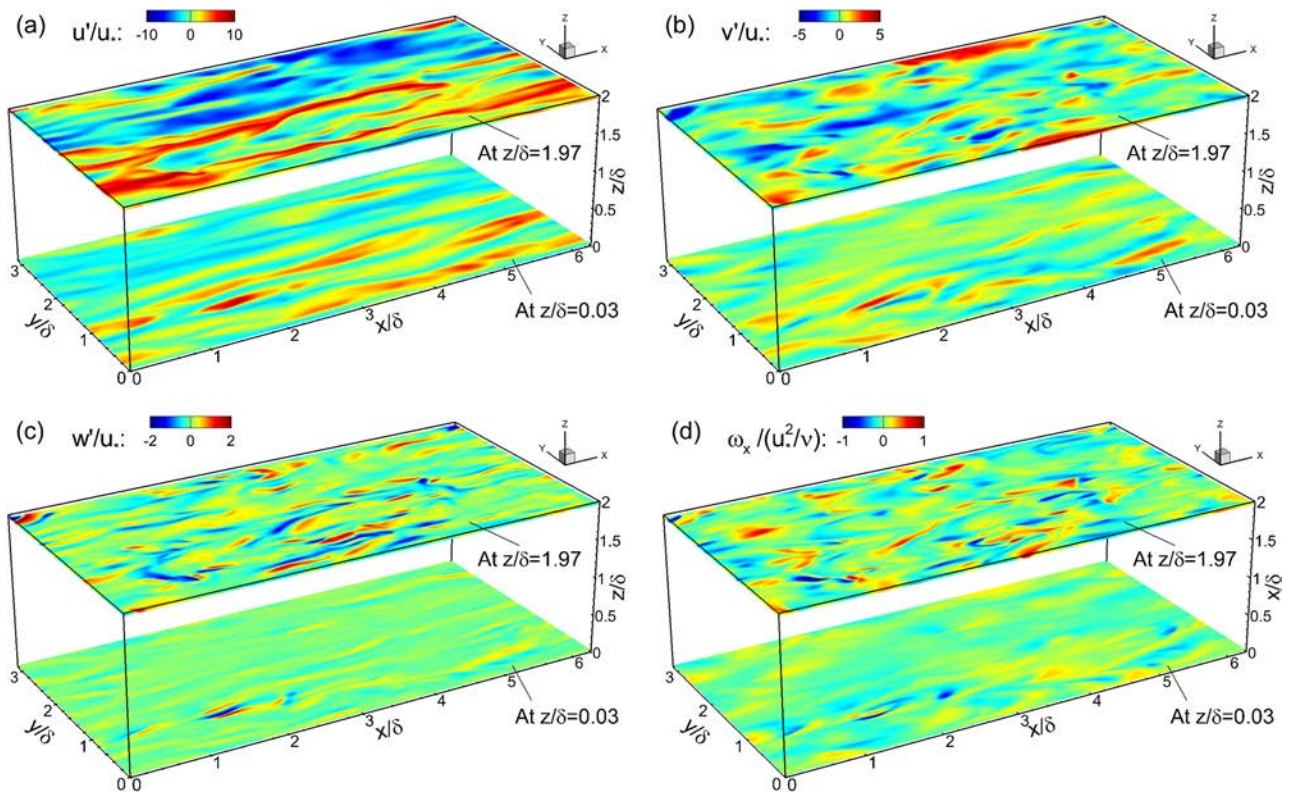


**FIG. 4.** Horizontal flow field near the bottom and top boundaries: (a) streamwise velocity fluctuation,  $u'$ ; (b) spanwise velocity fluctuation,  $v'$ ; (c) vertical velocity fluctuation,  $w'$ ; (d) streamwise vorticity,  $\omega_x$ . The velocity components are normalized by  $u_*$  and the vorticity is normalized by  $u_*^2/\nu$ . The two horizontal planes shown in the figure are at  $z = 0.03\delta$  and  $z = 1.97\delta$ , corresponding to  $z^+ = 5$  and  $(H - z)^+ = 5$ , respectively.

turbulence variances approach zero toward the bottom boundary due to the no-slip and impermeability conditions. The situation is not the same towards the top boundary, where the free-slip condition results in high values for  $\langle u'u' \rangle$  and  $\langle v'v' \rangle$ . The Reynolds shear

stress  $\langle u'w' \rangle$  exhibits a nearly constant value of about  $0.9u_*^2$  in the bulk flow region of the domain and approaches zero toward the two boundaries. The close-up view of the  $\langle u'w' \rangle$  profiles near the two boundaries shown in Fig. 7 indicates that the Reynolds shear

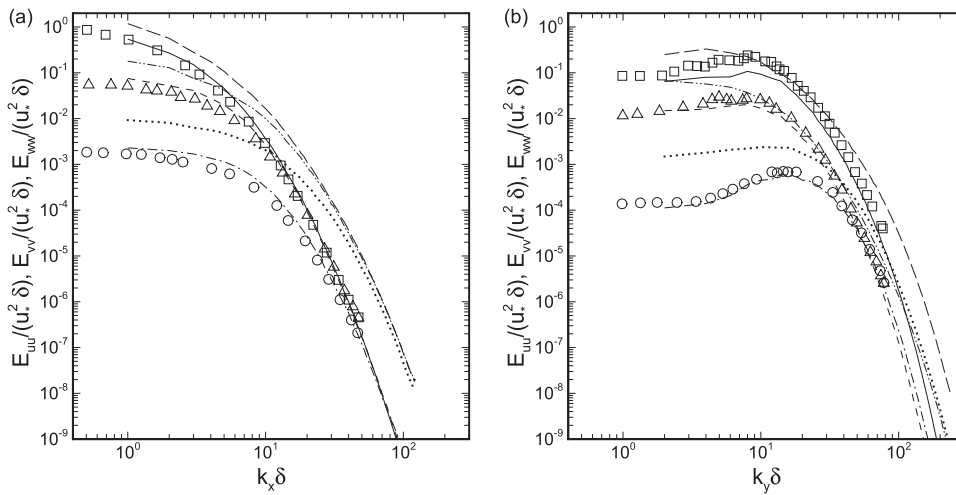


**FIG. 5.** One-dimensional energy spectra along the (a)  $x$ -direction and (b)  $y$ -direction. The spectra obtained from the current DNS case R1 are shown using different line patterns. At  $z^+ = 5$ : —,  $E_{uu}$ ; ---,  $E_{vv}$ ; -·-·,  $E_{wv}$ . At  $(H - z)^+ = 5$ : —,  $E_{uu}$ ; ---,  $E_{vv}$ ; ···,  $E_{wv}$ . The spectra at  $z^+ = 5$  obtained from the DNS of turbulent channel flow from Ref. 12 are also shown using open symbols:  $\square$ ,  $E_{uu}$ ;  $\triangle$ ,  $E_{vv}$ ;  $\circ$ ,  $E_{wv}$ .

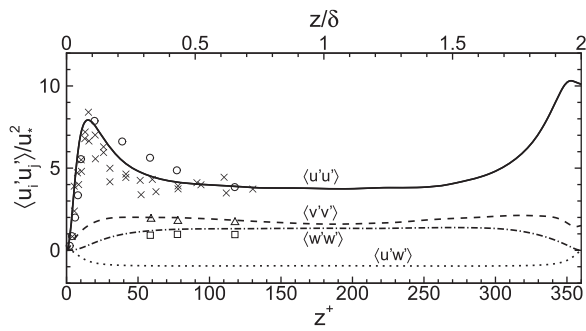


**FIG. 6.** Profiles of Reynolds stress components (normalized by  $u_*^2$ ) through the simulation domain height. Current DNS results are denoted by lines: —,  $\langle u'u' \rangle$ ; ---,  $\langle v'v' \rangle$ ; - - - ,  $\langle w'w' \rangle$ ; ···,  $\langle u'w' \rangle$ . Experimental data for plane turbulent Couette flow between two plates at  $Re_* = 434$  from Ref. 11 are denoted by symbols: ○,  $\langle u'u' \rangle$ ; △,  $\langle v'v' \rangle$ ; □,  $\langle w'w' \rangle$ . Experimental data for plane turbulent Couette flow between two plates at  $Re_* = 134$  from Ref. 13 are denoted by ×. Both  $z/\delta$  and the wall units  $z^+ = z/(v/u_*)$  are marked on the figure for the current DNS data, but the experimental data from the literature are plotted based on the wall units  $z^+$ .

stress approaches zero at different rates toward the two boundaries, with higher magnitude near the top free-slip boundary than near the bottom no-slip boundary at the same distance from the boundary.

The differences in the turbulence statistics near the bottom and top boundaries presented in this subsection can be rooted in the difference between the no-slip and free-slip conditions of the horizontal velocity fluctuations  $u'$  and  $v'$ . More detailed analyses are performed by focusing on the variations of the turbulent fluctuations of velocities in the near-boundary regions to help understand the different behaviors of the Reynolds stress components near the two different types of boundaries, which are discussed in detail in Subsection III B.

**B. Taylor series expansion analysis of fluctuating velocities**

The variation of velocity fluctuations in the near-boundary region can be analyzed using Taylor series expansion with respect to small  $z$  from the boundary.<sup>6,38</sup> In this subsection, we adopt this

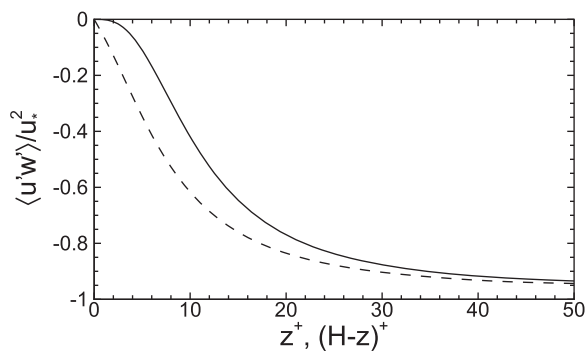


**FIG. 7.** Profiles of Reynolds shear stress  $\langle u'w' \rangle$  (normalized by  $u_*^2$ ) near the boundaries: —, bottom boundary; ---, top boundary.

analysis approach and apply it to study both the bottom and top boundary regions.

For a point near the bottom boundary (i.e., small  $z$ ) at  $(x, y, t)$ , the turbulent fluctuations of the three velocity components can be written in Taylor series as

$$u' = a_1 + b_1 z + c_1 z^2 + O(z^3), \tag{9}$$

$$v' = a_2 + b_2 z + c_2 z^2 + O(z^3), \tag{10}$$

$$w' = a_3 + b_3 z + c_3 z^2 + O(z^3). \tag{11}$$

By applying the no-slip boundary conditions  $u' = v' = 0$  at the bottom boundary  $z = 0$ , one can obtain  $a_1 = 0$  and  $a_2 = 0$  directly. The no-slip conditions also give  $\partial u'/\partial x = 0$  and  $\partial v'/\partial y = 0$ . Applying them to the continuity equation for fluctuating velocity gives

$$\frac{\partial w'}{\partial z} = -\left(\frac{\partial u'}{\partial x} + \frac{\partial v'}{\partial y}\right) = 0 \quad \text{at } z = 0, \tag{12}$$

resulting in  $b_3 = 0$ . The impermeability condition  $w' = 0$  at  $z = 0$  yields  $a_3 = 0$ .

By substituting these coefficients back to Eqs. (9)–(11) and by applying time and horizontal averaging, one can estimate the leading-order dependence of the Reynolds stress components  $\langle u_i' u_j' \rangle$  on  $z$  as<sup>6</sup>

$$\langle u'u' \rangle = \langle b_1^2 \rangle z^2 + O(z^3), \tag{13}$$

$$\langle v'v' \rangle = \langle b_2^2 \rangle z^2 + O(z^3), \tag{14}$$

$$\langle w'w' \rangle = \langle c_3^2 \rangle z^4 + O(z^5), \tag{15}$$

$$\langle u'w' \rangle = \langle b_1 c_3 \rangle z^3 + O(z^4). \tag{16}$$

As shown in Fig. 8, the profiles of  $\langle u_i' u_j' \rangle$  obtained from the current DNS obey these predicted  $z$ -dependence near the no-slip bottom boundary.

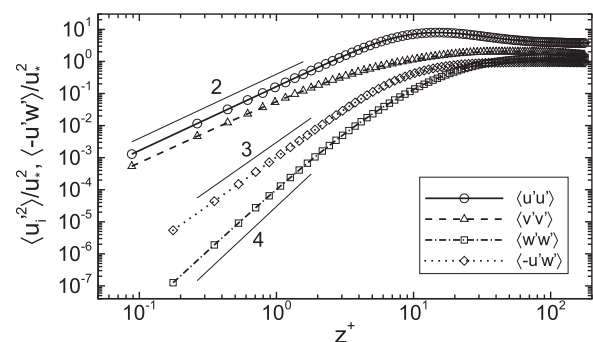


**FIG. 8.** Profiles of Reynolds stress components (normalized by  $u_*^2$ ) near the bottom boundary shown in the log-log scale. The values for  $\langle u'u' \rangle$  and  $\langle v'v' \rangle$  are evaluated on the regular grid points in  $z$ , and those for  $\langle w'w' \rangle$  and  $\langle -u'w' \rangle$  are evaluated on the staggered grid points in  $z$ , as shown by the open symbols in the figure. Reference lines for slopes 2, 3, and 4 are indicated by the thin solid lines in the figure.



Here, we can perform similar analysis for the velocity fluctuations near the free-slip top boundary. For a point near the top boundary (i.e., small  $z_t = H - z$ ) at  $(x, y, t)$ , the turbulent fluctuations of the three velocity components can be written in Taylor series as

$$u' = \alpha_1 + \beta_1 z_t + \gamma_1 z_t^2 + O(z_t^3), \quad (17)$$

$$v' = \alpha_2 + \beta_2 z_t + \gamma_2 z_t^2 + O(z_t^3), \quad (18)$$

$$w' = \alpha_3 + \beta_3 z_t + \gamma_3 z_t^2 + O(z_t^3). \quad (19)$$

Similar to that at the bottom boundary, the impermeability condition  $w' = 0$  at  $z_t = 0$  yields  $\alpha_3 = 0$ . The free-slip condition in the  $y$ -direction (i.e.,  $\partial v' / \partial z_t = 0$  at  $z_t = 0$ ) results in  $\beta_2 = 0$ . In the  $x$ -direction, the constant shear stress applied at the top boundary yields the following three conditions:

$$\left. \frac{\partial u'}{\partial z_t} \right|_{z_t=0} = \frac{\tau_x}{\mu}, \quad (20)$$

$$\left. \frac{\partial \langle u' \rangle}{\partial z_t} \right|_{z_t=0} = \frac{\tau_x}{\mu}, \quad (21)$$

$$\left. \frac{\partial u'}{\partial z_t} \right|_{z_t=0} = 0. \quad (22)$$

The free-slip condition Eq. (22) for  $u'$  yields  $\beta_1 = 0$ . Note that because of the free-slip conditions for  $u'$  and  $v'$  at the top boundary, the continuity equation  $\partial w' / \partial z_t = -(\partial u' / \partial x + \partial v' / \partial y)$  at  $z_t = 0$  does not give  $\partial w' / \partial z_t = 0$ . Therefore, the coefficient  $\beta_3$  is not zero in general, causing  $w'$  to behave differently near the top boundary than near the bottom boundary. Substituting  $\beta_1 = \beta_2 = \alpha_3 = 0$  back to Eqs. (17)–(19), we can obtain the following equations for Reynolds stress components  $\langle u'_i u'_j \rangle$  near the free-slip top boundary:

$$\langle u' u' \rangle = \langle \alpha_1^2 \rangle + 2\langle \alpha_1 \gamma_1 \rangle z_t^2 + O(z_t^3), \quad (23)$$

$$\langle v' v' \rangle = \langle \alpha_2^2 \rangle + 2\langle \alpha_2 \gamma_2 \rangle z_t^2 + O(z_t^3), \quad (24)$$

$$\langle w' w' \rangle = \langle \beta_3^2 \rangle z_t^2 + O(z_t^3), \quad (25)$$

$$\langle u' w' \rangle = \langle \alpha_1 \beta_3 \rangle z_t + O(z_t^2). \quad (26)$$

The above analysis based on Taylor series expansion shows that  $\langle u' u' \rangle$  and  $\langle v' v' \rangle$  are not zero at  $z_t = 0$  and vary according to  $z_t^2$  for small  $z_t$ . The vertical velocity variance  $\langle w' w' \rangle$  varies according to  $z_t^2$  near the free-slip top boundary, which is very different from the  $z^4$ -dependence near the no-slip bottom boundary. To the leading order in  $z_t$ , the Reynolds shear stress  $\langle u' w' \rangle$  is expected to vary linearly with  $z_t$  near the top boundary instead of the quadratic dependence  $z^2$  near the bottom boundary.

To check if the profiles of Reynolds stress components near the top boundary from the DNS results obey the scaling laws predicted by Eqs. (23)–(26), we define a generalized shape profile for each component as follows:

$$S(\langle u'_i u'_j \rangle)(z_t) = \langle u'_i u'_j \rangle(z_t) - \langle u'_i u'_j \rangle(z_t = 0), \quad (27)$$

$$S(\langle v' v' \rangle)(z_t) = -[\langle v' v' \rangle(z_t) - \langle v' v' \rangle(z_t = 0)], \quad (28)$$

$$S(\langle w' w' \rangle)(z_t) = \langle w' w' \rangle(z_t) - \langle w' w' \rangle(z_t = 0), \quad (29)$$

$$S(\langle u' w' \rangle)(z_t) = \langle u' w' \rangle(z_t) - \langle u' w' \rangle(z_t = 0). \quad (30)$$

These shape profiles eliminate the boundary values and convert the near-surface values to be positive, allowing us to plot the profiles in the log-log scale to examine the  $z_t$  dependence of the profiles near the free-slip boundary closely. Note that the additional negative sign on the right-hand side of Eq. (28) is included because  $\langle v' v' \rangle(z_t) < \langle v' v' \rangle(z_t = 0)$  for small  $z_t$  (see Fig. 6). As shown in Fig. 9, the generalized shape profiles obtained from the current DNS results agree with the  $\sim z_t^2$  scaling for  $\langle u' u' \rangle$ ,  $\langle v' v' \rangle$ , and  $\langle w' w' \rangle$  predicted by Eqs. (23)–(25) and the  $\sim z_t$  scaling predicted by Eq. (26).

### C. Turbulent kinetic energy budget

The mean turbulent kinetic energy (TKE) per unit mass is defined as  $k = (\langle u' u' \rangle + \langle v' v' \rangle + \langle w' w' \rangle) / 2$ , which includes three parts corresponding to the three velocity components. Under the statistically steady state, the balance equations for the three TKE components can be written as<sup>5</sup>

$$\begin{aligned} \frac{\overline{D}}{Dt} \left( \frac{\langle u' u' \rangle}{2} \right) = 0 = & \underbrace{-\langle u' w' \rangle \frac{\partial \langle u \rangle}{\partial z}}_{\mathcal{P}_1} - \underbrace{\nu \left( \frac{\partial u'}{\partial x} \frac{\partial u'}{\partial x} + \frac{\partial u'}{\partial y} \frac{\partial u'}{\partial y} + \frac{\partial u'}{\partial z} \frac{\partial u'}{\partial z} \right)}_{\mathcal{E}_1} \\ & + \underbrace{\nu \frac{\partial^2}{\partial z^2} \left( \frac{\langle u' u' \rangle}{2} \right)}_{\mathcal{D}_{v,1}} - \underbrace{\frac{\partial}{\partial z} \left( \frac{\langle u' u' w' \rangle}{2} \right)}_{\mathcal{T}_{v,1}} \\ & - \underbrace{\frac{\partial}{\partial x} \left( \frac{p'}{\rho} u' \right)}_{\mathcal{T}_{p,1}} + \underbrace{\left( \frac{p'}{\rho} \frac{\partial u'}{\partial x} \right)}_{\Pi_1}, \end{aligned} \quad (31)$$

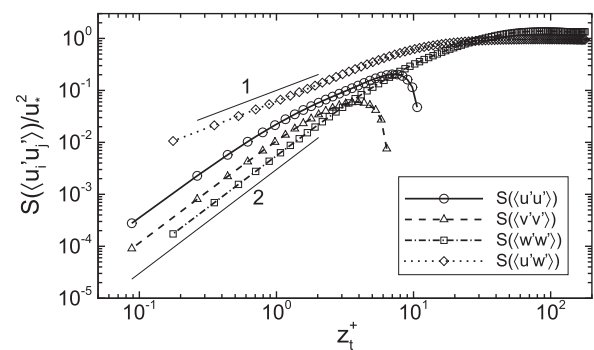


**FIG. 9.** Generalized shape profiles of Reynolds stress components (normalized by  $u_*^2$ ) near the top boundary shown in the log-log scale. The definitions of the generalized shape profiles  $S$  are given in Eqs. (27)–(30). The values for  $S(\langle u' u' \rangle)$  and  $S(\langle v' v' \rangle)$  are evaluated on the regular grid points in  $z$ , and those for  $S(\langle w' w' \rangle)$  and  $S(\langle u' w' \rangle)$  are evaluated on the staggered grid points in  $z$ , as shown by the open symbols in the figure. Reference lines for slopes 1 and 2 are indicated by the thin solid lines in the figure.

$$\begin{aligned}
 \frac{\overline{D}}{\overline{Dt}} \left( \frac{\langle v'v' \rangle}{2} \right) = & \underbrace{-\langle v'w' \rangle \frac{\partial \langle v \rangle}{\partial z}}_{\mathcal{P}_2} - \underbrace{v \left( \frac{\partial v'}{\partial x} \frac{\partial v'}{\partial x} + \frac{\partial v'}{\partial y} \frac{\partial v'}{\partial y} + \frac{\partial v'}{\partial z} \frac{\partial v'}{\partial z} \right)}_{\mathcal{E}_2} \\
 & + \underbrace{v \frac{\partial^2}{\partial z^2} \left( \frac{\langle v'v' \rangle}{2} \right)}_{\mathcal{D}_{v,2}} - \underbrace{\frac{\partial}{\partial z} \left( \frac{\langle v'v'w' \rangle}{2} \right)}_{\mathcal{T}_{i,2}} \\
 & - \underbrace{\frac{\partial}{\partial y} \left( \frac{p'}{\rho} v' \right)}_{\mathcal{T}_{p,2}} + \underbrace{\left( \frac{p'}{\rho} \frac{\partial v'}{\partial y} \right)}_{\Pi_2}, \quad (32)
 \end{aligned}$$

$$\begin{aligned}
 \frac{\overline{D}}{\overline{Dt}} \left( \frac{\langle w'w' \rangle}{2} \right) = & \underbrace{-\langle w'w' \rangle \frac{\partial \langle w \rangle}{\partial z}}_{\mathcal{P}_3} - \underbrace{v \left( \frac{\partial w'}{\partial x} \frac{\partial w'}{\partial x} + \frac{\partial w'}{\partial y} \frac{\partial w'}{\partial y} + \frac{\partial w'}{\partial z} \frac{\partial w'}{\partial z} \right)}_{\mathcal{E}_3} \\
 & + \underbrace{v \frac{\partial^2}{\partial z^2} \left( \frac{\langle w'w' \rangle}{2} \right)}_{\mathcal{D}_{v,3}} - \underbrace{\frac{\partial}{\partial z} \left( \frac{\langle w'w'w' \rangle}{2} \right)}_{\mathcal{T}_{i,3}} \\
 & - \underbrace{\frac{\partial}{\partial z} \left( \frac{p'}{\rho} w' \right)}_{\mathcal{T}_{p,3}} + \underbrace{\left( \frac{p'}{\rho} \frac{\partial w'}{\partial z} \right)}_{\Pi_3}. \quad (33)
 \end{aligned}$$

Here,  $\overline{D}/\overline{Dt} = \partial/\partial t + \langle \mathbf{u} \rangle \cdot \nabla$  is the material derivative based on the mean flow velocity. For the time and horizontal average  $\langle f \rangle$  of the physical quantity  $f$  under the statistically steady state,  $\partial \langle f \rangle / \partial t = 0$ ,  $\partial \langle f \rangle / \partial x = 0$ ,  $\partial \langle f \rangle / \partial y = 0$ , and  $\langle w \rangle = 0$ , which give  $\overline{D} \langle f \rangle / \overline{Dt} = 0$  for the left-hand side of each balance equation. The TKE budget terms are denoted as follows:  $\mathcal{P}$  for the production terms,  $\mathcal{E}$  for the dissipation terms,  $\mathcal{D}_v$  for the molecular diffusion terms,  $\mathcal{T}_i$  for the turbulent transport terms,  $\mathcal{T}_p$  for the pressure transport terms, and  $\Pi$  for the pressure redistribution terms. The subscripts “1,” “2,” and “3” indicate the terms in the  $x$ -,  $y$ -, and  $z$ -directions, respectively.

In Eqs. (31)–(33), all the budget terms are listed including the ones that have zero value, i.e.,  $\mathcal{T}_{p,1}$ ,  $\mathcal{P}_2$ ,  $\mathcal{T}_{p,2}$ , and  $\mathcal{P}_3$ . Adding these three equations together gives the balance equation for the total TKE,<sup>5,6</sup>

$$\begin{aligned}
 \frac{\overline{D}k}{\overline{Dt}} = 0 = & \underbrace{-\langle u'w' \rangle \frac{\partial \langle u \rangle}{\partial z}}_{\mathcal{P}} - \underbrace{\frac{\partial}{\partial z} \left( \frac{p'}{\rho} w' \right)}_{\mathcal{T}_p} + \underbrace{v \frac{\partial^2 k}{\partial z^2}}_{\mathcal{D}_v} - \underbrace{\frac{1}{2} \frac{\partial \langle w' \mathbf{u}' \cdot \mathbf{u}' \rangle}{\partial z}}_{\mathcal{T}_i} \\
 & - \underbrace{v \langle \nabla \mathbf{u}' : (\nabla \mathbf{u}')^T \rangle}_{\mathcal{E}}, \quad (34)
 \end{aligned}$$

where the budget terms are denoted using consistent symbols as in Eqs. (31)–(33) but for the total TKE  $k$ . Also, note that the summation of the three pressure redistribution terms is typically not listed in the balance equation of  $k$  because  $\Pi = \sum_{i=1}^3 \Pi_i = \langle \frac{p'}{\rho} \nabla \cdot \mathbf{u}' \rangle = 0$  for incompressible flows. The pressure redistribution terms  $\Pi_i$  are responsible for redistribution the TKE among different velocity components, but the net effect on the balance of total TKE  $k$  is zero.

Figure 10 shows the profiles of the budget terms in Eq. (34) in the viscous boundary layers near the bottom and top boundaries. The current DNS results for the bottom no-slip boundary region show good agreement with the results from Ref. 12 based on DNS of turbulent channel flow at the same Reynolds number of  $Re_* = 180$ . The separated budget balances in the three directions for the current DNS according to Eqs. (31)–(33) are shown in Fig. 11. For the no-slip boundary region, the production of TKE occurs in the  $x$ -direction with the peak located at  $z^+ \approx 12$ . Around its peak region, the TKE production is balanced by dissipation, turbulent transport, and viscous diffusion. The dissipations in the  $x$ - and  $y$ -directions increase toward the maximum values on the no-slip boundary where the contributions mainly come from  $\langle (\partial u' / \partial z)^2 \rangle$  in  $\mathcal{E}_1$  and  $\langle (\partial v' / \partial z)^2 \rangle$  in  $\mathcal{E}_2$  near the no-slip boundary. The turbulence transports TKE toward both the boundary and the outer region, while the viscous diffusion transports TKE mainly toward the boundary to balance the maximum dissipation on the boundary.<sup>6</sup> In the outer region toward the middle of the simulation domain, the production is mostly balanced by the dissipation. The profiles

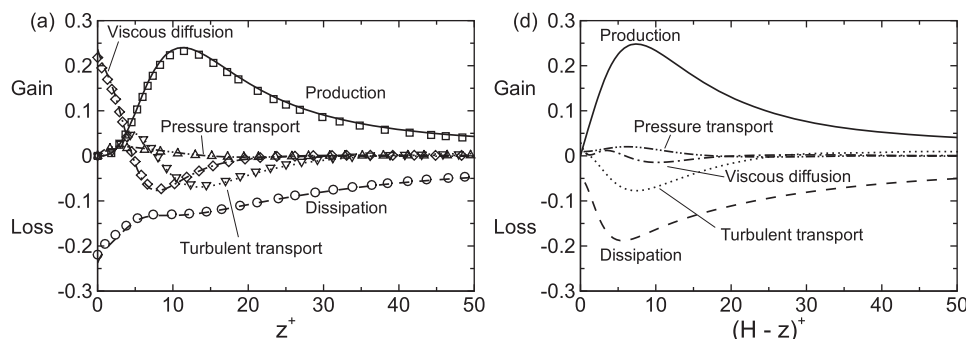


**FIG. 10.** Budget of turbulent kinetic energy  $k$  near the (a) no-slip bottom boundary and (b) shear-driven free-slip top boundary. Different budget terms are shown using different line patterns: —, production  $\mathcal{P}$ ; ---, dissipation  $\mathcal{E}$ ; ···, turbulent transport  $\mathcal{T}_i$ ; —·—, viscous diffusion  $\mathcal{D}_v$ ; — — —, pressure transport  $\mathcal{T}_p$ . DNS data from Ref. 12 (reproduced based on Fig. 7.18 of Ref. 6) are also denoted in panel (a) by symbols:  $\square$ , production;  $\circ$ , dissipation;  $\nabla$ , turbulent transport;  $\diamond$ , viscous diffusion;  $\triangle$ , pressure transport.

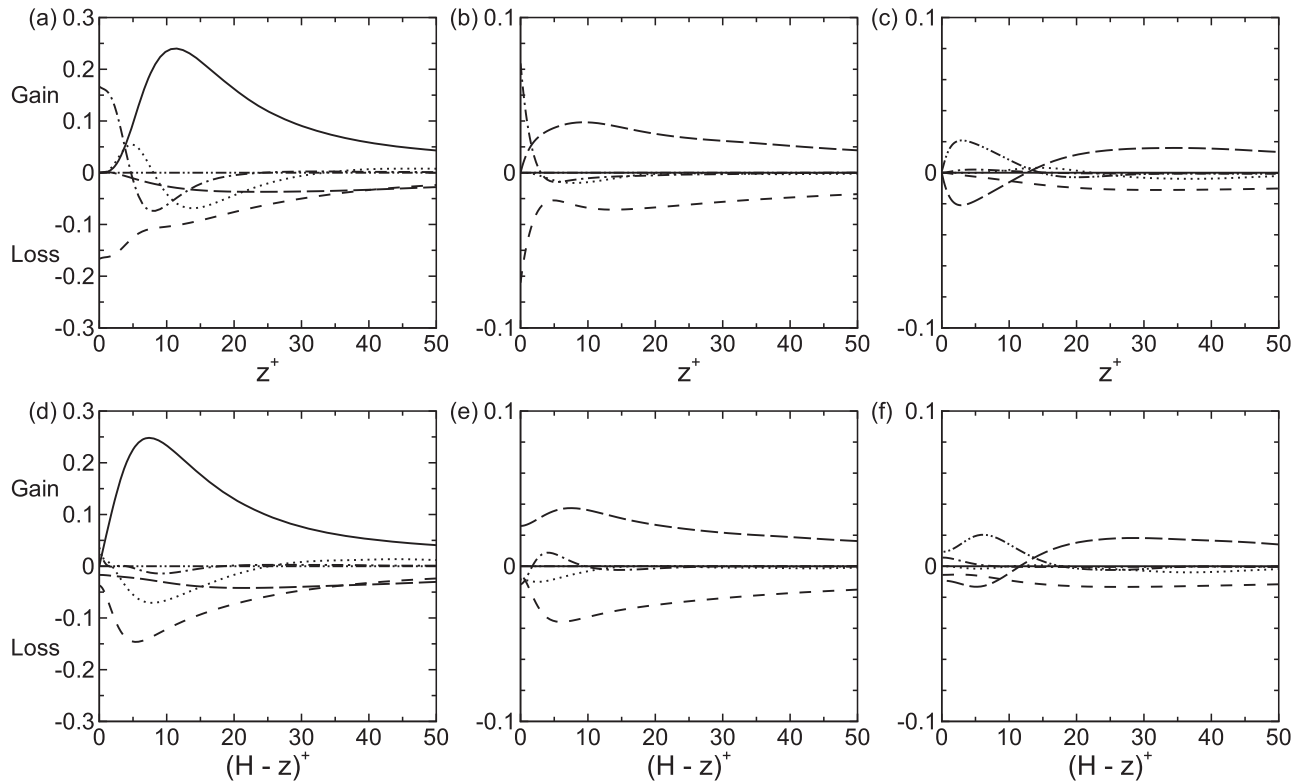


**FIG. 11.** Budgets of TKE components near the (a)–(c) no-slip bottom boundary and (d)–(f) shear-driven free-slip top boundary. The budget balance in three directions are shown in three columns: (a) and (d) are for the  $x$ -direction; (b) and (e) are for the  $y$ -direction; (c) and (f) are for the  $z$ -direction. Different budget terms are shown using different line patterns: —, production  $\mathcal{P}_i$ ; ---, dissipation  $\mathcal{E}_i$ ; ···, turbulent transport  $\mathcal{T}_{t,i}$ ; -·-, viscous diffusion  $\mathcal{D}_{v,i}$ ; — — —, pressure transport  $\mathcal{T}_{p,i}$ ; — — —, pressure redistribution  $\Pi_i$ . Note that the vertical axes in different columns have different ranges.

of the pressure redistribution terms shown in Fig. 11 indicate that the TKE is converted from the  $x$ - and  $z$ -directions into the  $y$ -direction in the near-surface region, and from the  $x$ -direction into both the  $y$ - and  $z$ -directions at  $z^+ \gtrsim 13$ .

In contrast, the TKE balance near the free-slip boundary shows apparent differences compared to the no-slip boundary region. The production of TKE also occurs in the  $x$ -direction but its peak is located at  $z_t^+ = (H - z)^+ \approx 7$ . Around its peak region, the TKE production is mostly balanced by dissipation and turbulent transport. Toward the free-slip boundary, the dissipations in the  $x$ - and  $y$ -directions decrease to relatively small but nonzero values, for which the main contributions come from the nonzero  $\langle (\partial u'/\partial x)^2 + (\partial u'/\partial y)^2 \rangle$  in  $\mathcal{E}_1$  and  $\langle (\partial v'/\partial x)^2 + (\partial v'/\partial y)^2 \rangle$  in  $\mathcal{E}_2$  while both  $\partial u'/\partial z$  and  $\partial v'/\partial z$  become zero due to the free-slip condition. The pressure redistribution terms in the top free-slip boundary region show similar general trends as their counterparts in the bottom no-slip boundary region, but all have nonzero values at the free-slip boundary due to the nonzero  $p'$  and  $\partial w'/\partial z$  there.

Unlike at the no-slip boundary where the dissipation is balanced by viscous diffusion in both the  $x$ - and  $y$ -directions, at the free-slip boundary the balances in the three directions are different. In the  $x$ -direction [Fig. 11(d)], at  $z_t^+ = (H - z)^+ = 0$ , the dissipation

$\mathcal{E}_1$  together with a negative pressure redistribution  $\Pi_1$  are balanced by the viscous diffusion  $\mathcal{D}_{v,1}$  and a small but nonzero turbulent transport  $\mathcal{T}_{t,1}$ . Note that  $\mathcal{T}_{t,1}$  can be rewritten as

$$\mathcal{T}_{t,1} = -\frac{\partial}{\partial z} \left( \frac{\langle u'u'w' \rangle}{2} \right) = -\left\langle w' \frac{\partial}{\partial z} \left( \frac{u'u'}{2} \right) \right\rangle - \left\langle \left( \frac{u'u'}{2} \right) \frac{\partial w'}{\partial z} \right\rangle. \quad (35)$$

Unlike at the no-slip bottom boundary where  $\mathcal{T}_{t,1} = 0$  because  $u' = w' = 0$  and  $\partial w'/\partial z = 0$  [see Eq. (12)], at the free-slip top boundary

$$\mathcal{T}_{t,1} = -\left\langle \left( \frac{u'u'}{2} \right) \frac{\partial w'}{\partial z} \right\rangle = \langle \alpha_1^2 \beta_3 \rangle \quad \text{at } z_t = (H - z) = 0 \quad (36)$$

according to Eqs. (17) and (19). In the  $y$ -direction [Fig. 11(e)], at  $z_t^+ = (H - z)^+ = 0$  the flow gains TKE through a positive pressure redistribution  $\Pi_2$ , balanced by the combined effect of dissipation  $\mathcal{E}_2$ , viscous diffusion  $\mathcal{D}_{v,2}$  and turbulent transport  $\mathcal{T}_{t,2}$  that have comparable magnitudes. Finally in the  $z$ -direction [Fig. 11(f)], at  $z_t^+ = (H - z)^+ = 0$  the flow gains TKE through the pressure transport  $\mathcal{T}_{p,3}$  and viscous diffusion  $\mathcal{D}_{v,3}$ , balanced by the dissipation  $\mathcal{E}_3$  and pressure redistribution  $\Pi_3$ . Overall, the differences between the free-slip and no-slip boundary conditions induce considerable differences in the TKE balance statistics even though the background mean flow (i.e.,

the mean streamwise velocity profiles) have considerable similarities [Fig. 3(b)].

#### D. Statistics of vorticity fluctuations and vortex structures

When analyzing the complex flow physics in turbulent flows, coherent vortex structures are often found to provide valuable insights for the three-dimensional characteristics of the turbulence field.<sup>39,40</sup> The differences between the no-slip and free-slip boundary conditions also affect the characteristics of the vorticity field and coherent vortex structures in the turbulent boundary layer. While the vorticity of the flow field can be calculated directly based on the curl of the velocity vector obtained from the DNS, the coherent flow structures in the turbulence need to be defined and identified based on a certain algorithm. In this paper, we adopt the widely used  $\lambda_2$  method<sup>41</sup> for identifying and visualizing the coherent vortex structures in the turbulence. In particular, letting  $\mathbf{S}$  and  $\mathbf{\Omega}$  being the symmetric and antisymmetric parts of the velocity gradient tensor  $\nabla\mathbf{u}$ ,  $\lambda_2$  is the second largest eigenvalue of the tensor  $\mathbf{S}^2 + \mathbf{\Omega}^2$ . The vortex structures can then be visualized using the isosurfaces of negative  $\lambda_2$ .<sup>41</sup> In this subsection, we take a close look of the characteristics of the vortical structures near the two types of boundaries based on both the vorticity and  $\lambda_2$  fields.

Figure 12 shows the two-dimensional contours of the vorticity components ( $\omega_x, \omega'_y, \omega_z$ ) on the ( $x, z$ )- and ( $y, z$ )-planes, where  $\omega_x$  and  $\omega_z$  are the instantaneous vorticity components in the  $x$ - and  $z$ -directions and  $\omega'_y = \omega_y - \langle \omega_y \rangle$  is the turbulent fluctuation of the instantaneous vorticity  $\omega_y$  in the  $y$ -direction. Note that in the turbulent Couette flow considered in this study, the mean vorticities satisfy  $\langle \omega_x \rangle = 0$ ,  $\langle \omega_y \rangle \neq 0$ , and  $\langle \omega_z \rangle = 0$ . Thus ( $\omega_x, \omega'_y, \omega_z$ ) represent the vorticity components associated with the turbulent fluctuations of the velocity field. Near the no-slip bottom boundary,

the vorticity field obtained from the current DNS exhibits several representative vortical structures found in previous studies of wall turbulence,<sup>39</sup> e.g., the contour-rotating streamwise vortex pair marked in Fig. 12(a) and the hairpin vortices marked in Fig. 12(c). Note that the hairpin vortices are organized in packet and their heads (marked by the arrows) are aligned with an inclined shear layer of strong positive  $\omega'_y$  associated with the ejection of low-speed fluid flow from the boundary, which is consistent with the hairpin vortex autogeneration and organization mechanism found in previous studies.<sup>40,42–44</sup> Note that the autogeneration mechanism of vortical structures by existing vortical structures in wall turbulence requires the presence of the no-slip wall for new structures to be formed and rolled up from the wall. In contrast, no clear sign of hairpin vortex packets is observed near the free-slip top boundary in Fig. 12(c). Note that the fluctuation of the spanwise vorticity satisfies  $\omega'_y = \partial u' / \partial z - \partial w' / \partial x = 0$  at the top boundary as a result of the free-slip condition, but is significant at the no-slip bottom boundary due to the large values of  $\partial u' / \partial z$  associated with the near-wall turbulence events such as sweeps and ejections.<sup>12,39</sup>

The streamwise vortical structures also interact differently with the no-slip and free-slip boundaries. Figure 13 shows the zoom-in views of the two flow regions highlighted in Fig. 12(a). The instantaneous vortices are visualized using the  $\lambda_2$  method discussed above. Note that each of the two streamwise vortices in Fig. 13(a) generates a streamwise vorticity field of opposite sign on the bottom boundary due to the no-slip condition.<sup>12</sup> Note that the streamwise vortices can also appear individually instead of in pair<sup>39</sup> and interact similarly with the no-slip boundary. In contrast, the streamwise vortex shown in Fig. 13(b) does not generate opposite streamwise vorticity on the top boundary because the free-slip results in  $\omega_x = \partial w / \partial y - \partial v / \partial z = 0$ . Opposite to the situation for the other two vorticity components, the vertical vorticity  $\omega_z = \partial v / \partial x - \partial u / \partial y$  is

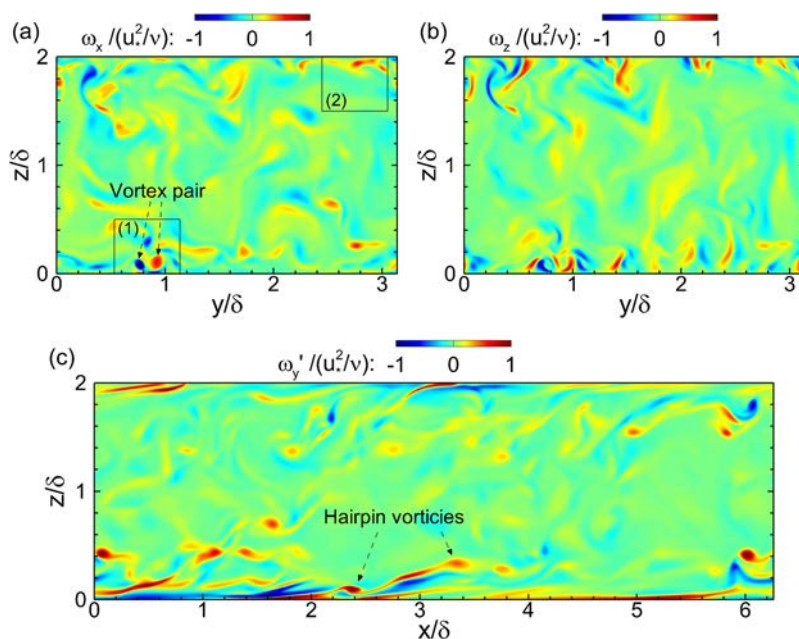


**FIG. 12.** Vorticity field from DNS case R1: (a)  $\omega_x$  on the ( $y, z$ )-plane at  $x = 1.8\delta$ ; (b)  $\omega_z$  on the ( $y, z$ )-plane at  $x = 1.8\delta$ ; and (c)  $\omega'_y$  on the ( $x, z$ )-plane at  $y = 0.8\delta$ . The vorticities are normalized by  $u_*^2/\nu$ . Two sample regions (1) and (2) are marked in (a) and their corresponding zoom-in views are shown in Fig. 13.

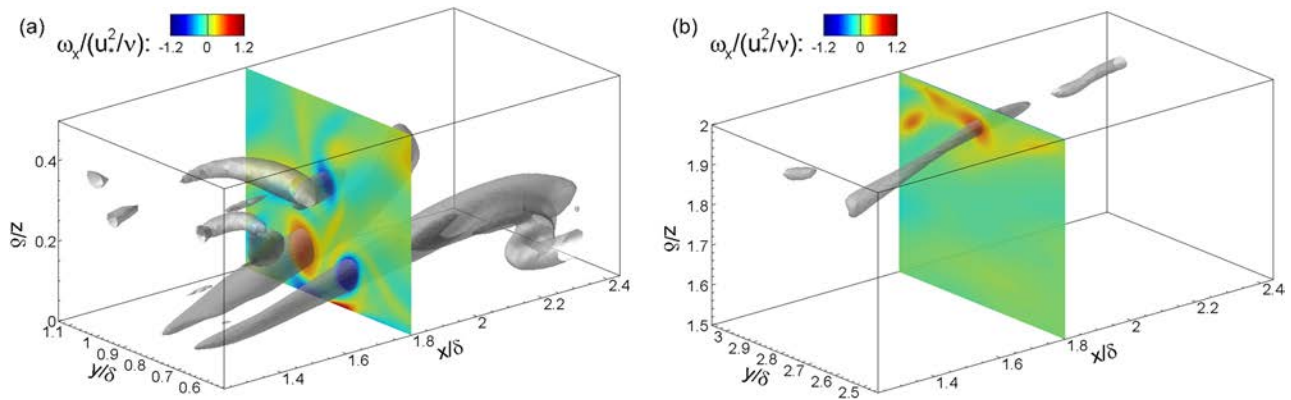


**FIG. 13.** Zoom-in view of the flow fields around the regions (1) and (2) marked in Fig. 12(a). (a) is for region (1) and (b) is for region (2). The contours of  $\omega_x$  (normalized by  $u_*^2/\nu$ ) are shown on the  $(y, z)$ -plane at  $x = 1.8\delta$  in each panel. The instantaneous three-dimensional vortex structures are visualized using the isosurfaces of  $\lambda_2 = -0.05$  (in gray color).

zero at the no-slip boundary but can be significant at the free-slip boundary where  $u$  and  $v$  are allowed to vary horizontally. This can be seen from Fig. 12(b), in which the  $\omega_z$  contours vanish toward the bottom boundary but remain significant toward the top boundary.

The different characteristics of the vorticity fields near the two types of boundaries can also be analyzed statistically. Figure 14 shows the profiles of the root-mean-square (rms) vorticity fluctuations  $\langle \omega'_i \rangle_{rms}$  and also compares the values near the bottom no-slip boundary from the current DNS with the DNS results of Ref. 12 and experimental data of Ref. 45 for fully developed turbulent channel flows. Good agreement is found between the current DNS results and the data from the literature. Figure 14 also shows clearly that towards the free-slip top boundary  $\langle \omega'_x \rangle_{rms}$  and  $\langle \omega'_y \rangle_{rms}$  become zero while  $\langle \omega'_z \rangle_{rms}$  is significant, which are opposite to the counterparts near the no-slip bottom boundary where  $\langle \omega'_x \rangle_{rms}$  and  $\langle \omega'_y \rangle_{rms}$

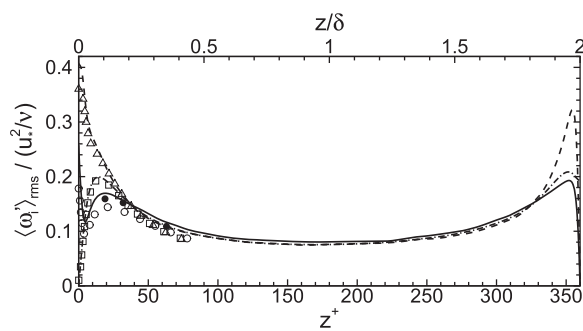


**FIG. 14.** Profiles of root-mean-square vorticity fluctuations (normalized by  $u_*^2/\nu$ ). Results based on the current DNS case R1 are denoted by lines: —,  $\langle \omega'_x \rangle_{rms}$ ; ---,  $\langle \omega'_y \rangle_{rms}$ ; - · -,  $\langle \omega'_z \rangle_{rms}$ . DNS results for channel flow from DNS data from Ref. 12 are denoted by open symbols:  $\circ$ ,  $\langle \omega'_x \rangle_{rms}$ ;  $\Delta$ ,  $\langle \omega'_y \rangle_{rms}$ ;  $\square$ ,  $\langle \omega'_z \rangle_{rms}$ . Experimental data of  $\langle \omega'_z \rangle_{rms}$  for turbulent channel flow from Ref. 45 are denoted by  $\bullet$ . Both  $z/\delta$  and the wall units  $z^+ = z/(v/u_*)$  are marked on the figure for the current DNS data, but the DNS and experimental data from the literature are plotted based on the wall units  $z^+$ .

have their maximum values at the boundary but  $\langle \omega'_z \rangle_{rms}$  becomes zero.

Quantifying the characteristics of the coherent vortex structures in turbulent flows are often very challenging, as illustrated by the complexity of the instantaneous vortex field shown in Fig. 15. Conditional averaging techniques have been shown to provide valuable information about the characteristics of coherent flow structures in turbulent flows.<sup>46–49</sup> In this study, we employ the variable-interval space-averaging (VISA) method<sup>47</sup> to identify the representative coherent vortex structures in the flow regions near the bottom and top boundaries and elucidate the effects of different boundary conditions on the characteristics of the vortices. As shown in Fig. 15, the quasistreamwise vortices are the dominant vortex structures near both the bottom and top boundaries. Following Refs. 47 and 49, we define the VISA value of the streamwise vorticity as

$$\widehat{\omega}_x(x, y, z, t, W_x, W_y) \equiv \frac{1}{4W_x W_y} \int_{x-W_x}^{x+W_x} \int_{y-W_y}^{y+W_y} \omega_x(\xi, \psi, z, t) d\xi d\psi, \quad (37)$$

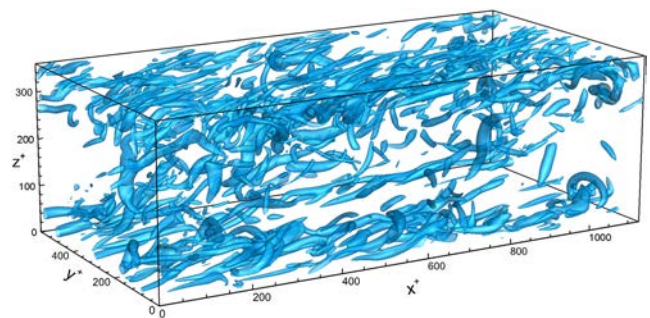


**FIG. 15.** Instantaneous vortex structures from case R1 visualized using the isosurface of  $\lambda_2 = -0.02$ .

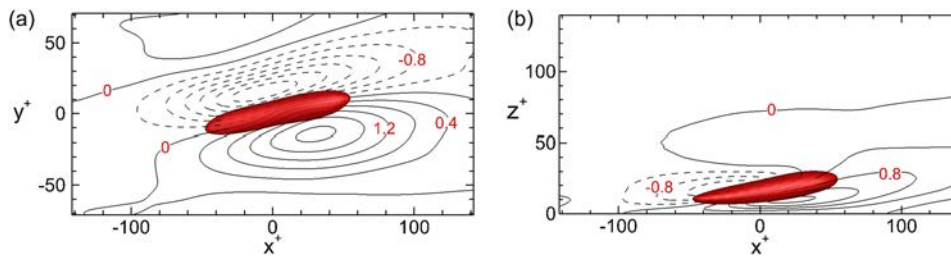


**FIG. 16.** Conditionally averaged vortex structure near the bottom boundary obtained by the applying VISA method based on positive streamwise vorticity  $\omega_x$ . The vortex structure is visualized using the isosurface of  $\lambda_2 = -0.02$ . (a) shows the top view with the contour lines of  $u'/u_*$  shown on the  $(x, y)$ -plane at  $z^+ = 15$ , and (b) shows the side view with the contour lines of  $u'/u_*$  shown on the  $(x, z)$ -plane at the center of the conditional average domain. The contour levels have a fixed interval of 0.4.

where  $W_x$  and  $W_y$  are the half-widths of the horizontal averaging window for VISA, and are set to 70 and 35 wall units in this study, respectively. The local variance of  $\omega_x$  is then calculated as

$$\omega_x^{\text{var}}(x, y, z, t) \equiv \omega_x^2(x, y, z, t) - \widehat{\omega_x^2}(x, y, z, t, W_x, W_y). \tag{38}$$

Samples for conditional average are detected by applying the following criterion at a detection height  $z_d$ :

$$\mathcal{D}(x, y, z_d, t) = \begin{cases} 1, & \text{if } \omega_x^{\text{var}}(x, y, z_d, t) > c[(\omega'_x)_{\text{rms}}(z_d)]^2 \text{ and } \omega_x(x, y, z_d, t) > 0, \\ 0, & \text{otherwise.} \end{cases} \tag{39}$$

In the current analysis, the threshold level for the criterion is set to be  $c = 10$ . The detection vertical level is set to be  $z_d^+ = 15$  for conditional sampling near the bottom boundary, and  $(H - z_d)^+ = 8$  for the top boundary, which are chosen based on the two peaks of  $(\omega'_x)_{\text{rms}}$  shown in Fig. 14. We use 90 three-dimensional instantaneous snapshots obtained from the DNS separated by a constant time interval of  $\Delta t^+ = \Delta t / (\nu / u_*^2) = 14$ . Based on Eq. (39), a total of 57 163 samples are identified near the bottom boundary and 59 227 samples are taken near the top boundary.

Figures 16 and 17 show the VISA conditionally averaged flow structures deduced from the instantaneous flow fields near the bottom and top boundaries, respectively. In both figures, a well-organized quasistreamwise vortex with  $\omega_x > 0$  is obtained from the conditional average. As shown in Fig. 16(a), the vortex near the bottom boundary induces positive  $u'$  on its right side (when viewed

from the top) due to sweep of high-speed flow toward the boundary and negative  $u'$  on its left side due to the ejection of low-speed flow away from the near-boundary region. Although Fig. 17(a) shows a similar general flow pattern for the top boundary case, in this case the positive  $u'$  on its right side corresponds to the “ejection” of high-speed flow away from the top free-slip boundary and the negative  $u'$  on its left side corresponds to the “sweep” of low-speed flow towards the top boundary due to the local mean velocity gradient near the top boundary (see Fig. 3). It is also worth mentioning that both Figs. 16(a) and 17(a) indicate that the averaged streamwise vortex has a nonzero inclination angle on the horizontal plane with respect to the streamwise direction  $x$ , but the angle for the vortex near the no-slip boundary is much larger than that for the free-slip case, i.e.,  $12^\circ$  in Fig. 16(a) vs  $5^\circ$  in Fig. 17(a).

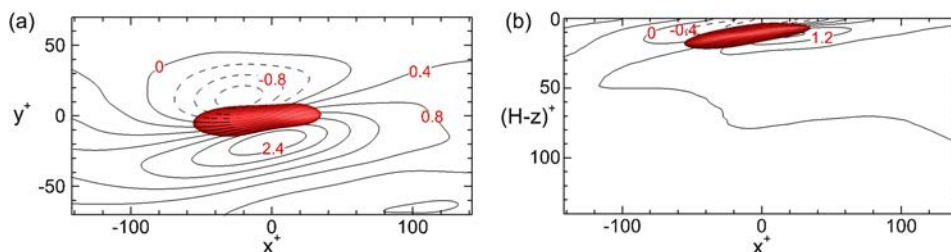


**FIG. 17.** Conditionally averaged vortex structure near the top boundary obtained by applying the VISA method based on positive streamwise vorticity  $\omega_x$ . The vortex structure is visualized using the isosurface of  $\lambda_2 = -0.02$ . (a) shows the top view with the contour lines of  $u'/u_*$  shown on the  $(x, y)$ -plane at  $(H - z)^+ = 8$ , and (b) shows the side view with the contour lines of  $u'/u_*$  shown on the  $(x, z)$ -plane at the center of the conditional average domain. The contour levels have a fixed interval of 0.4.

The vertical distances of the conditionally averaged vortices to the corresponding boundaries also appear to be different, with a smaller distance for the vortex next to the free-slip top boundary as shown in Fig. 17. This is not surprising because of the differences in the detection vertical levels  $z_d^+ = 15$  and  $(H - z_d)^+ = 8$  used in the VISA for the bottom and top boundaries, respectively, which are chosen based on the profiles of  $\langle \omega_x' \rangle_{rms}$  (Fig. 14). The combined effect of this closer distance and the free-slip boundary condition turns out to significantly increase the computational cost for DNS of shear turbulence with free-slip boundary, which is discussed in Subsection III E.

The differences in the inclination angle and vertical distance observed from the conditional average results in Figs. 16 and 17 can be linked back to how the vortices interact with different types of boundaries. As shown in Fig. 13(a), a streamwise vortex in the near-boundary region can generate a secondary rotational flow field

adjacent to the bottom boundary with opposite sign of  $\omega_x$  due to the no-slip condition.<sup>12</sup> The mutual induction between these primary and secondary streamwise vortices causes the inclination of the primary vortex in the horizontal plane and lifts it further away from the no-slip boundary.<sup>42,50</sup> The lack of the generation of the secondary streamwise vorticity on the free-slip boundary significantly weakens the mutual induction between the vortex structure and the top boundary, resulting in smaller horizontal inclination angle and vertical distance from the free-slip boundary.

### E. Effect of free-slip boundary condition on computational cost

The DNS results presented in Secs. III A–III D show apparent differences in the statistics of shear turbulence near the free-slip and no-slip boundaries, which can also impose different computational requirements on the DNS in order to properly resolve these different

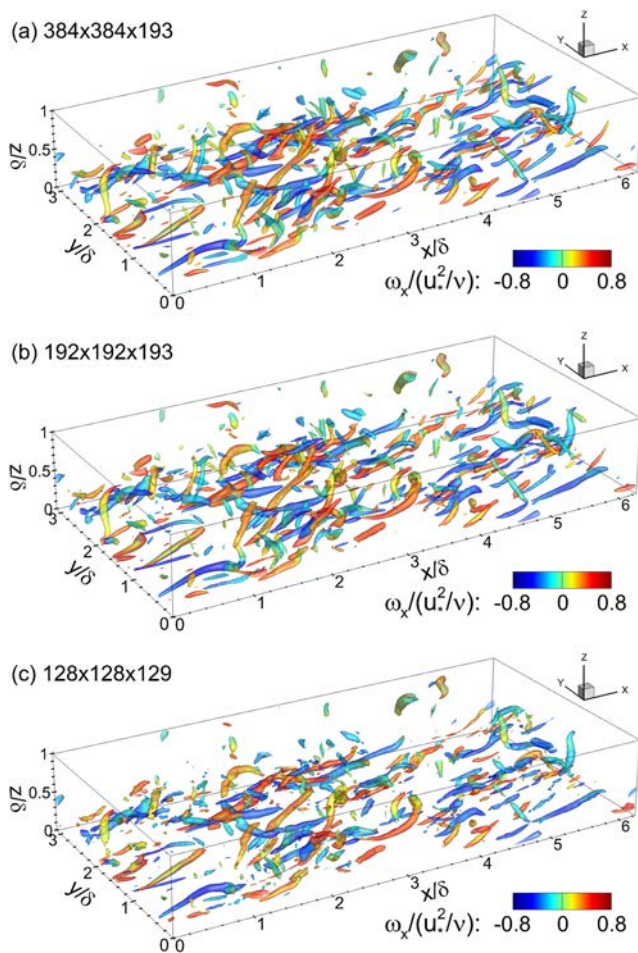


**FIG. 18.** Comparison of instantaneous vortex structures near the bottom boundary obtained from DNS with different grid numbers: (a) case R1 with  $384 \times 384 \times 193$  grid points; (b) case R2 with  $192 \times 192 \times 193$  grid points; and (c) case R3 with  $128 \times 128 \times 129$  grid points. The bottom half-domain of  $0 \leq z \leq H/2$  is shown for each case. The vortices are visualized using the isosurfaces of  $\lambda_2 = -0.04$  and colored based on the value of  $\omega_x$ . Both  $\lambda_2$  and  $\omega_x$  are presented in wall units.

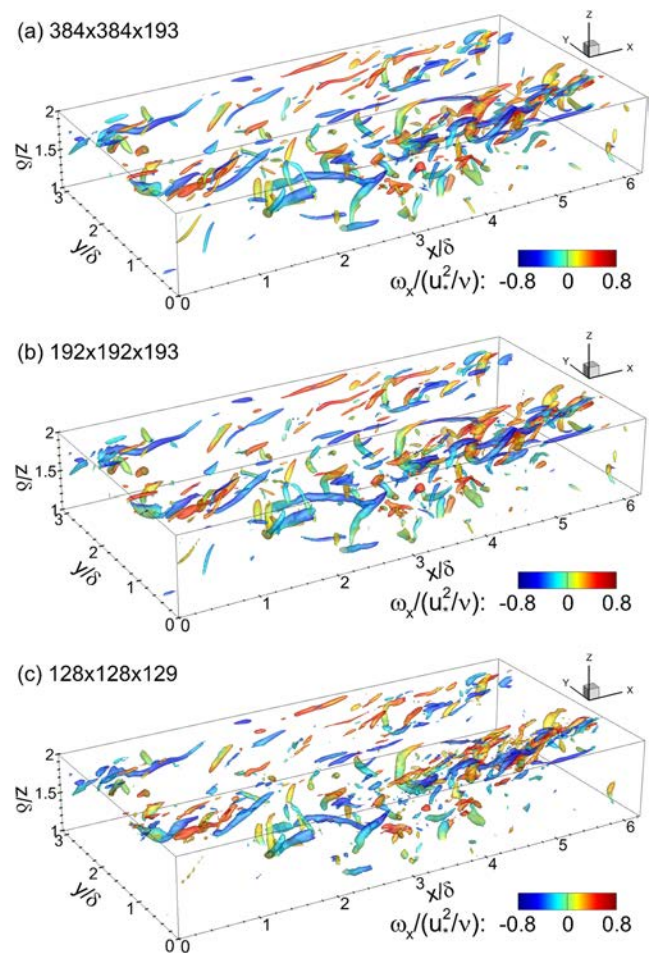


**FIG. 19.** Comparison of instantaneous vortex structures near the top boundary obtained from DNS with different grid numbers: (a) case R1 with  $384 \times 384 \times 193$  grid points; (b) case R2 with  $192 \times 192 \times 193$  grid points; and (c) case R3 with  $128 \times 128 \times 129$  grid points. The top half-domain of  $H/2 \leq z \leq H$  is shown for each case. The vortices are visualized using the isosurfaces of  $\lambda_2 = -0.04$  and colored based on the value of  $\omega_x$ . Both  $\lambda_2$  and  $\omega_x$  are presented in wall units.

flow features. To check the effect of the free-slip boundary condition on the computational cost of DNS, in this section we present and discuss the simulation results of cases R1, R2, and R3 that are obtained using different grid resolutions. Case R1 has the finest grid resolutions in all the three directions among the three cases. Case R2 has identical vertical grid resolution as case R1, but uses coarser grid resolutions in the horizontal directions (i.e., twice the sizes of  $\Delta x^+$  and  $\Delta y^+$  used in case R1). Case R3 has coarser grid resolutions in all the three directions than cases R1 and R2. In order to make a direct comparison, all three cases use the same instantaneous flow field obtained from case R1 as the initial condition, with the lower resolution initial conditions for cases R1 and R2 constructed by truncating the additional Fourier modes in the  $x$ - and  $y$ -directions, as well as linear interpolation in the  $z$ -direction (for case R3 due to its different vertical grid resolution from case R1).

For comparison, Fig. 18 shows the instantaneous vortex structures near the bottom boundary from the three cases after the flow fields are advanced in time by 50 viscous time units. For all the three different grid resolutions considered in cases R1–R3, the vortex structures near the bottom no-slip boundary are well resolved by the DNS. Near the free-slip boundary, the situation becomes quite different. As shown in Fig. 19, the primary DNS case R1 can resolve the vortex structures smoothly with its high grid resolution, but the other two lower resolution cases showing sign of numerical instability. The visualized instantaneous vortices in Fig. 19(c) show

that the grid resolution used in case R3 is insufficient to resolve the small-scale features of the vortex structures very close to the free-slip boundary, resulting in shattering of vortex structures.

Figures 20 and 21 show contours of the velocity and vorticity components on the horizontal plane at  $(H - z)^+ = 5.4$  obtained from the three DNS cases, respectively. The primary DNS case R1 shows smooth results for both the velocity and vorticity fields resolved by its high grid resolution. The lower resolution cases R2 and R3 exhibit clear numerical oscillations that can be seen from the unsmooth velocity and vorticity contours, for which some sample regions are marked in Figs. 20 and 21 for demonstration purpose.

The effects of the horizontal grid resolutions on the DNS results from cases R1–R3 can also be seen from the energy spectra. Figure 22 shows the one-dimensional streamwise and spanwise turbulent kinetic energy spectra of the three velocity components near the no-slip bottom boundary at  $z^+ = 5$ . The spectra from the lower resolution cases R2 and R3 show good agreement with the higher resolution case R1, and there is no clear pileup of turbulent kinetic energy at the high wavenumbers. For comparison, Fig. 23 shows the corresponding spectra near the free-slip top boundary at  $(H - z)^+ = 5$ . Although the spectra from cases R2 and R3 show good agreement with that from case R1 at low wavenumbers, the two lower resolutions cases do exhibit clear energy pileup at high wavenumbers, suggesting the insufficient horizontal grid resolutions for resolving the turbulent fluctuations at small length scales.

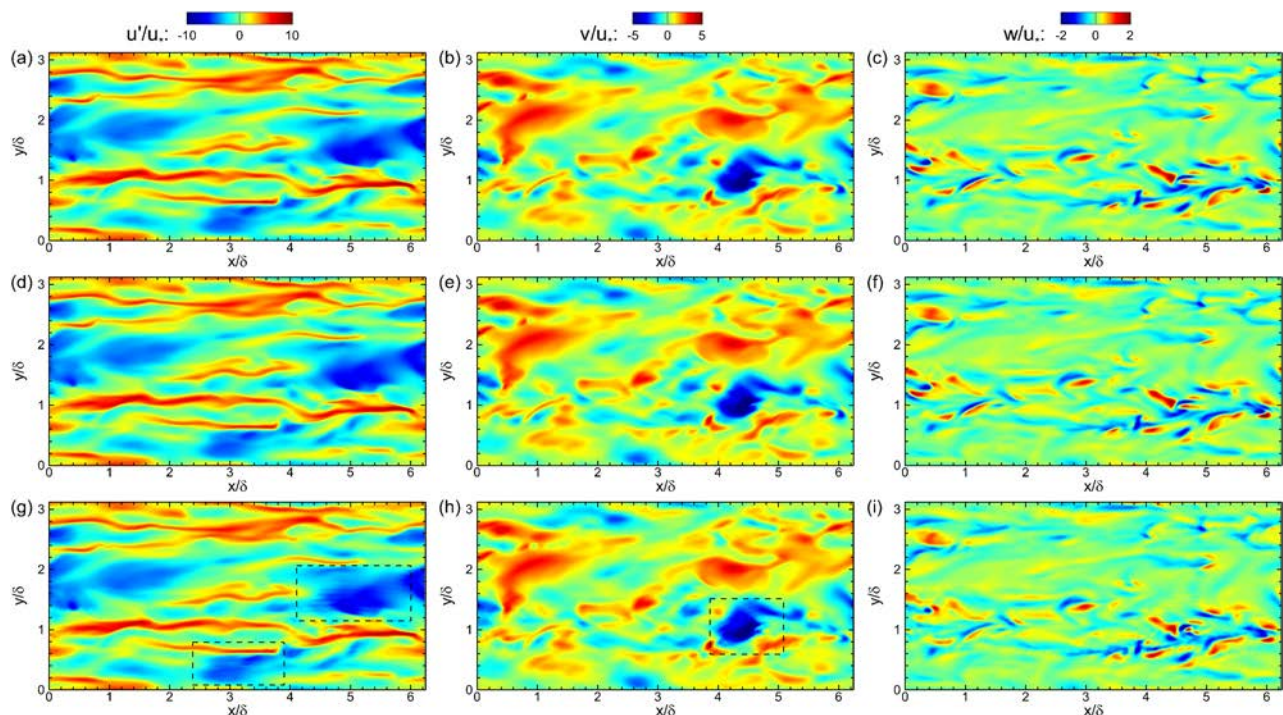


**FIG. 20.** Comparison of instantaneous velocities on the  $(x, y)$ -plane at  $(H - z)^+ = 5.4$  obtained from DNS with different grid resolutions: [(a)–(c)] case R1; [(d)–(f)] case R2; and [(g)–(i)] case R3. Three different velocity components are shown: (a), (d), and (g) for streamwise velocity fluctuation  $u'$ ; (b), (e), and (h) for spanwise velocity  $v$ ; (c), (f), and (i) for vertical velocity  $w$ . The velocity components are normalized by  $u_*$ . Some sample regions of unsmooth velocity fields in case R3 are marked by the rectangular boxes with black dashed lines in (g) and (h).



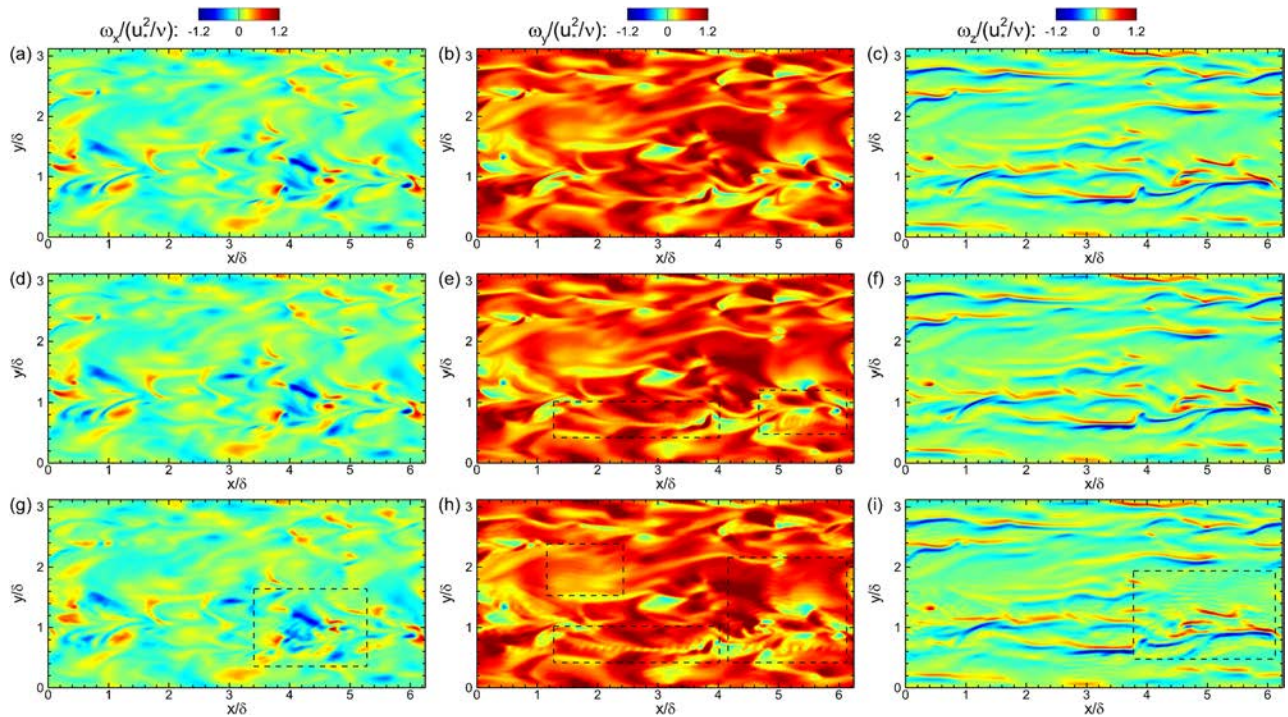


**FIG. 21.** Comparison of instantaneous vorticities on the  $(x, y)$ -plane at  $(H - z)^+ = 5.4$  obtained from DNS with different grid resolutions: [(a)–(c)] case R1; [(d)–(f)] case R2; and [(g)–(i)] case R3. Three different vorticity components are shown: (a), (d), and (g) for streamwise vorticity  $\omega_x$ ; (b), (e), and (h) for spanwise vorticity  $\omega_y$ ; and (c), (f), and (i) for vertical vorticity  $\omega_z$ . The vorticity components are normalized by  $u_*^2/\nu$ . Some sample regions of unsmooth vorticity fields in cases R2 and R3 are marked by the rectangular boxes with black dashed lines in (e) and (g)–(i).

Overall, the comparisons of the instantaneous flow structures near the bottom and top boundaries obtained from the three different DNS grid resolutions indicate that it is computationally much more expensive to smoothly resolve the turbulent flow physics near a free-slip boundary than near a no-slip boundary. Note that the case R3 has comparable grid resolution as other prior DNS studies of turbulent flows over no-slip boundary (see Table I) and is found

to well capture the essential turbulent flow structures near the bottom boundary in the current DNS [Fig. 18(c)]. Case R2 has identical vertical grid resolution as case R1 but with lower horizontal grid resolutions and is unable to obtain smooth flow field as in case R1. This suggests that increased grid resolutions are needed in the horizontal directions to resolve the small-scale flow features occurring near the free-slip top boundary. Note that the TKE budget analysis results

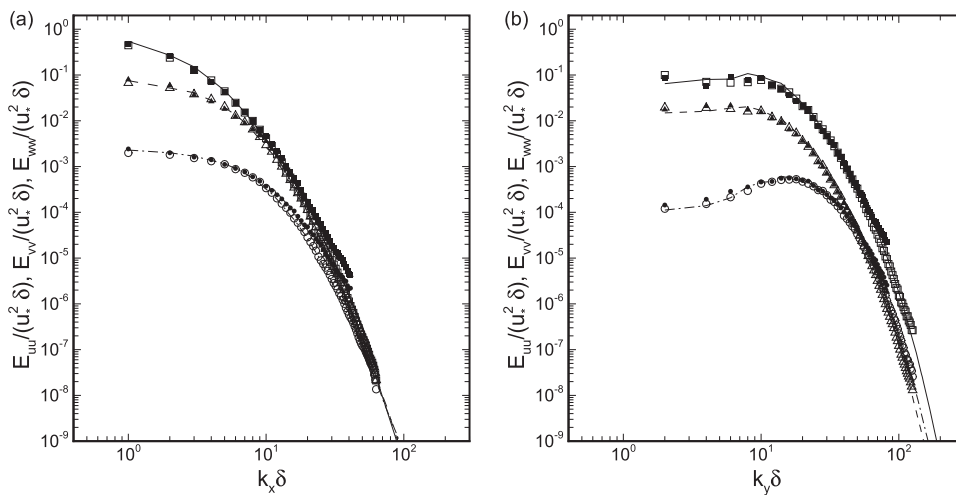


**FIG. 22.** One-dimensional energy spectra near the no-slip bottom boundary at  $z^+ = 5$  along the (a)  $x$ -direction and (b)  $y$ -direction. For case R1 with  $384 \times 384 \times 193$  grid points: —,  $E_{uu}$ ; ---,  $E_{vv}$ ; - - -,  $E_{wv}$ . For case R2 with  $192 \times 192 \times 193$  grid points: □,  $E_{uu}$ ; △,  $E_{vv}$ ; ○,  $E_{wv}$ . For case R3 with  $128 \times 128 \times 129$  grid points: ■,  $E_{uu}$ ; ▲,  $E_{vv}$ ; ●,  $E_{wv}$ .

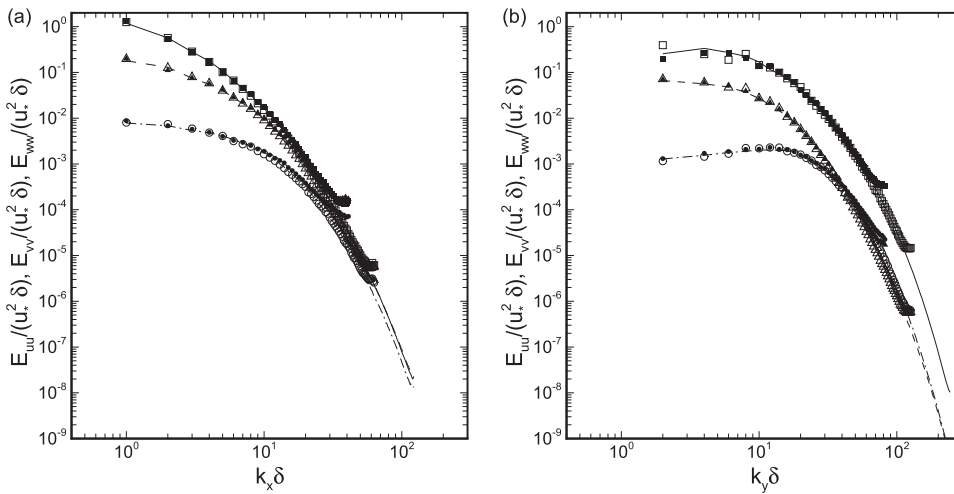


**FIG. 23.** One-dimensional energy spectra near the free-slip top boundary at  $(H - z)^+ = 5$  along the (a)  $x$ -direction and (b)  $y$ -direction. For case R1 with  $384 \times 384 \times 193$  grid points: —,  $E_{uu}$ ; ---,  $E_{vv}$ ; -·-,  $E_{ww}$ . For case R2 with  $192 \times 192 \times 193$  grid points: □,  $E_{uu}$ ; △,  $E_{vv}$ ; ○,  $E_{ww}$ . For case R3 with  $128 \times 128 \times 129$  grid points: ■,  $E_{uu}$ ; ▲,  $E_{vv}$ ; ●,  $E_{ww}$ .

shown in Figs. 10 and 11 indicate that the magnitudes of the viscous diffusion and dissipation are large near the no-slip boundary, but become small toward the free-slip boundary. The lower intensities for the viscous diffusion and dissipation allow the small-scale turbulent fluctuations to remain energetic very close to the free-slip boundary, which may demand finer horizontal grid resolutions to resolve them.

**IV. CONCLUSIONS**

In this study, we perform DNS to study the effects of a free-slip boundary on the characteristics of shear turbulence. We set up an idealized flow system in the DNS with a no-slip impermeable bottom boundary and a free-slip impermeable top boundary. The flow is driven by a constant shear stress imposed on the top boundary in the  $x$ -direction, which generates a Couette type turbulent flow in the simulation with a friction Reynolds number of  $Re_* = 180$ . Such a flow configuration provides both no-slip and free-slip boundaries with identical friction velocity so that the turbulent flow statistics near the two types of boundaries can be compared to help understand the effect of free-slip boundary on shear turbulence.

Using the DNS data, the statistics of the turbulent flow are studied systematically. Comparison of the turbulence statistics reveals that the free-slip condition of the top boundary causes considerable differences in both the mean and fluctuating velocities compared to the no-slip boundary case. The mean velocity profile near the free-slip boundary exhibits a similar basic structure as the counterpart near the no-slip boundary, i.e., a linear profile in the viscous sub-layer and a logarithmic profile in the log-law region. However, near the free-slip boundary, the viscous sublayer only extends to about  $z^+ \approx 2$ , which is smaller than the classical value of  $z^+ \approx 5$  for the no-slip boundary case. The profile offset constant for the logarithmic profile in the free-slip condition case also has a smaller value of  $B \approx 2$  compared to  $B \approx 5$  for the no-slip boundary case.

Statistical analysis and theoretical prediction based Taylor series expansion show that the Reynolds stress components also have different dependences on the vertical coordinate near the no-slip and free-slip boundaries. Near the no-slip boundary, all the Reynolds

stress components are zero at the boundary and scale as  $\langle u'u' \rangle(z) \sim z^2$ ,  $\langle v'v' \rangle(z) \sim z^2$ ,  $\langle w'w' \rangle(z) \sim z^4$ , and  $\langle u'w' \rangle(z) \sim z^3$  for small  $z$ . Near the free-slip boundary where  $z_t = H - z$  is small,  $\langle u'u' \rangle$  and  $\langle v'v' \rangle$  are not zero at the boundary and scale as  $[\langle u'u' \rangle(z_t) - \langle u'u' \rangle(z_t = 0)] \sim z_t^2$  and  $[\langle v'v' \rangle(z_t) - \langle v'v' \rangle(z_t = 0)] \sim z_t^2$  with a similar quadratic profile shape as near the no-slip boundary; the other two Reynolds stress components near the free-slip boundary behave very differently from the counterparts near the no-slip boundary, following  $\langle w'w' \rangle(z_t) \sim z_t^2$  and  $\langle u'w' \rangle(z_t) \sim z_t$  for small  $z_t$ . Further analysis on the TKE balances also reveals considerable differences in the behaviors of TKE budget terms near the no-slip and free-slip boundaries.

The free-slip condition of the top boundary in the current flow configuration also affects how vortical structures interact with the boundary. While the streamwise vorticity  $\omega_x$  and spanwise vorticity fluctuation  $\omega'_y$  are zero at the free-slip boundary, the vertical vorticity  $\omega_z$  is not zero and can vary in space and time. This is opposite to the situation at the no-slip boundary where  $\omega_x$  and  $\omega'_y$  are large and  $\omega_z = 0$ . Direct observation of the instantaneous vortices in the simulated flow field and conditional averaging based on the VISA method show that the dominant vortex structures, i.e., quasistreamwise vortices, have different horizontal inclination angles with respect to the streamwise direction and different vertical distances from the neighboring boundaries in the no-slip and free-slip boundary cases. The VISA averaged vortex from the free-slip boundary region has a smaller inclination angle (i.e., more aligned with the streamwise direction) and is located closer to boundary than its counterpart in the no-slip boundary region.

Finally, the different velocity boundary conditions induced by the free-slip and no-slip boundaries impose different computational requirements on DNS. The relatively weak dissipation of turbulence near the free-slip boundary results in higher turbulence intensity and smaller scale flow features than those near the no-slip boundary, which can significantly increase the computational cost of DNS in order to smoothly resolve turbulent flow field near the free-slip surface. The comparison of DNS results near the two types of boundaries reported in this study suggests that cautions should be taken when setting up future DNS runs of shear-driven turbulence over

free-slip surface if one wants to choose the DNS grid resolutions based on previously reported DNS runs of no-slip boundary cases.

**ACKNOWLEDGMENTS**

This research was supported by Di Yang’s start-up funds at the University of Houston. The authors acknowledge the use of the Opuntia Cluster and the advanced support from the Core Facility for Advanced Computing and Data Science at the University of Houston to carry out the numerical simulations presented here.

**APPENDIX: VERTICAL COMPUTATIONAL GRID DISTRIBUTION**

In the current DNS, a staggered vertical grid system is used for spatial discretization in the  $z$ -direction. More details of the

staggered grid system can be found in Ref. 34. The vertical grids are not evenly spaced and are clustered towards the bottom and top boundaries where the vertical gradient of the streamwise velocity is large.

For a vertical grid point with index  $k$ , the corresponding vertical coordinate  $z(k)$  and grid space  $\Delta z(k)$  are calculated according to

$$z(k) = \frac{\zeta(k) - \zeta(1)}{\zeta(N_z) - \zeta(1)} H, \tag{A1}$$

$$\Delta z(k) = z(k + 1) - z(k), \tag{A2}$$

where  $\zeta(1) = 0$  and  $\zeta(k) = \zeta(1) + \sum_{i=1}^{k-1} \Delta\zeta(k)$  for  $1 < k \leq N_z$ . The spacing function  $\Delta\zeta(k)$  is defined as

$$\Delta\zeta(k) = \begin{cases} \frac{\{1 - \cos[2\pi\xi(k)]\}(\gamma - 1)}{2} + 1, & \text{if } N_b \leq k \leq N_z - N_b, \\ \zeta(N_b), & \text{if } 1 < k < N_b \text{ or } N_z - N_b < k < N_z - 1, \\ \zeta(N_b)/2, & \text{if } k = 1, \\ \zeta(N_b)/2, & \text{if } k = N_z - 1, \end{cases} \tag{A3}$$

where

$$\xi(k) = \frac{1}{2} \left\{ 1 + \frac{\sinh[\beta(2\eta(k) - 1)]}{\sinh(\beta)} \right\}, \tag{A4}$$

$$\eta(k) = \frac{k - N_b}{N_z - 2N_b}. \tag{A5}$$

The grid clustering is controlled by two parameters, i.e.,  $\beta$  for the range of clustering and  $\gamma$  for the largest grid space ratio. The first  $N_b = 4$  grid points near the bottom and top boundaries are spaced equally to allow simplification of the finite difference scheme near the boundaries. Figure 24 illustrates the vertical grid clustering based on  $N_z = 65$ . Three different combinations of  $(\beta, \gamma)$  are shown.

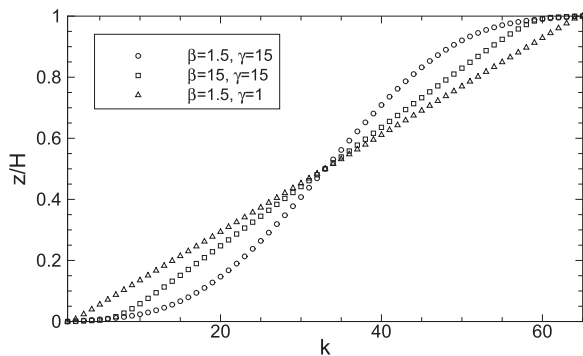


**FIG. 24.** Illustration of vertical grid clustering for  $N_z = 65$ . The normalized vertical coordinate  $z/H$  is plotted as a function of the grid index  $k$ .

When  $\gamma = 1$ , the grids are evenly spaced. In this study, the vertical grids for the three DNS cases are all generated according to the above grid clustering functions with  $(\beta, \gamma) = (1.5, 15)$  based on the corresponding vertical grid numbers  $N_z$  shown in Table I.

**REFERENCES**

- <sup>1</sup> P. P. Sullivan and J. C. McWilliams, “Dynamics of winds and currents coupled to surface waves,” *Annu. Rev. Fluid Mech.* **42**, 19 (2010).
- <sup>2</sup> J. C. McWilliams, P. P. Sullivan, and C.-H. Moeng, “Langmuir turbulence in the ocean,” *J. Fluid Mech.* **334**, 1 (1997).
- <sup>3</sup> P. P. Sullivan, J. C. McWilliams, and W. K. Melville, “Surface gravity wave effects in the oceanic boundary layer: Large-eddy simulation with vortex force and stochastic breakers,” *J. Fluid Mech.* **593**, 405 (2007).
- <sup>4</sup> Y. Noh, G. Goh, S. Raasch, and M. Gryschka, “Formation of a diurnal thermocline in the ocean mixed layer simulated by LES,” *J. Phys. Oceanogr.* **39**, 1244 (2009).
- <sup>5</sup> H. Tennekes and J. Lumley, *A First Course in Turbulence* (MIT Press, Cambridge, MA, 1972).
- <sup>6</sup> S. B. Pope, *Turbulent Flows* (Cambridge University Press, 2000).
- <sup>7</sup> R. A. Handler, T. F. Swain, Jr., R. I. Leighton, and J. D. Swearingen, “Length scales and the energy balance for turbulence near a free surface,” *AIAA J.* **31**, 1998 (1993).
- <sup>8</sup> D. T. Walker, R. I. Leighton, and L. O. Garza-Rios, “Shear-free turbulence near a flat free surface,” *J. Fluid Mech.* **320**, 19 (1996).
- <sup>9</sup> L. Shen, X. Zhang, D. K. P. Yue, and G. S. Triantafyllou, “The surface layer for free-surface turbulent flows,” *J. Fluid Mech.* **386**, 167 (1999).
- <sup>10</sup> A. Kermani, H. R. Khakpour, L. Shen, and T. Igusa, “Statistics of surface renewal of passive scalars in free-surface turbulence,” *J. Fluid Mech.* **678**, 379–416 (2011).
- <sup>11</sup> M. M. M. El Telbany and A. J. Reynolds, “The structure of turbulent plane Couette,” *J. Fluids Eng.* **104**, 367 (1982).

- <sup>12</sup>J. Kim, P. Moin, and R. Moser, "Turbulence statistics in fully developed channel flow at low Reynolds number," *J. Fluid Mech.* **177**, 133 (1987).
- <sup>13</sup>E. M. Aydin and H. J. Leutheusser, "Plane-Couette flow between smooth and rough walls," *Exp. Fluids* **11**, 302 (1991).
- <sup>14</sup>D. V. Papavassiliou and T. J. Hanratty, "Interpretation of large-scale structures observed in a turbulent plane Couette flow," *Int. J. Heat Fluid Flow* **18**, 55 (1997).
- <sup>15</sup>R. D. Moser, J. Kim, and N. N. Mansour, "Direct numerical simulation of turbulent channel flow up to  $Re_\tau = 590$ ," *Phys. Fluids* **11**, 943 (1999).
- <sup>16</sup>P. P. Sullivan, J. C. McWilliams, and C.-H. Moeng, "Simulation of turbulent flow over idealized water waves," *J. Fluid Mech.* **404**, 47 (2000).
- <sup>17</sup>B. Debusschere and C. J. Rutland, "Turbulent scalar transport mechanisms in plane channel and Couette flows," *Int. J. Heat Mass Transfer* **47**, 1771 (2004).
- <sup>18</sup>S. Hoyas and J. Jiménez, "Scaling of the velocity fluctuations in turbulent channels up to  $Re_\tau = 2003$ ," *Phys. Fluids* **18**, 011702 (2006).
- <sup>19</sup>M. Lee and R. D. Moser, "Direct numerical simulation of turbulent channel flow up to  $Re_\tau \approx 5200$ ," *J. Fluid Mech.* **774**, 395 (2015).
- <sup>20</sup>J. U. Bretheim, C. Meneveau, and D. F. Gayme, "Standard logarithmic mean velocity distribution in a band-limited restricted nonlinear model of turbulent flow in a half-channel," *Phys. Fluids* **27**, 011702 (2015).
- <sup>21</sup>S. Komori, R. Nagaosa, Y. Murakami, S. Chiba, K. Ishii, and K. Kuwahara, "Direct numerical simulation of three-dimensional open-channel flow with zero-shear gas-liquid interface," *Phys. Fluids A* **5**, 115 (1993).
- <sup>22</sup>R. A. Handler, J. R. Saylor, R. I. Leighton, and A. L. Rovelstad, "Transport of a passive scalar at a shear-free boundary in fully developed turbulent open channel flow," *Phys. Fluids* **11**, 2607 (1999).
- <sup>23</sup>H. R. Khakpour, L. Shen, and D. K. P. Yue, "Transport of passive scalar in turbulent shear flow under a clean or surfactant-contaminated free surface," *J. Fluid Mech.* **670**, 527–557 (2011).
- <sup>24</sup>X. Guo and L. Shen, "Interaction of a deformable free surface with statistically-steady homogeneous turbulence," *J. Fluid Mech.* **658**, 33 (2010).
- <sup>25</sup>X. Guo and L. Shen, "Numerical study of the effect of surface waves on turbulence underneath. Part 1. Mean flow and turbulence vorticity," *J. Fluid Mech.* **733**, 558 (2013).
- <sup>26</sup>P. R. Gent and P. A. Taylor, "A numerical model of the air flow above water waves," *J. Fluid Mech.* **77**, 105 (1976).
- <sup>27</sup>P. Y. Li, D. Xu, and P. A. Taylor, "Numerical modeling of turbulent airflow over water waves," *Boundary-Layer Meteorol.* **95**, 397 (2000).
- <sup>28</sup>N. Kihara, H. Hanazaki, T. Mizuya, and H. Ueda, "Relationship between airflow at the critical height and momentum transfer to the traveling waves," *Phys. Fluids* **19**, 015102 (2007).
- <sup>29</sup>S. Leibovich, "The form and dynamics of Langmuir circulation," *Annu. Rev. Fluid Mech.* **15**, 391–427 (1983).
- <sup>30</sup>S. A. Thorpe, "Langmuir circulation," *Annu. Rev. Fluid Mech.* **36**, 55–79 (2004).
- <sup>31</sup>S. A. Orszag, "Transform method for calculation of vector coupled sums: Application to the spectral form of the vorticity equation," *J. Atmos. Sci.* **27**, 890 (1970).
- <sup>32</sup>C. Canuto, M. Yousuff Hussaini, A. Quarteroni, and T. A. Zang, Jr., *Spectral Methods in Fluid Dynamics*, Springer Series in Computational Physics (Springer, 1988).
- <sup>33</sup>J. Kim and P. Moin, "Application of a fractional-step method to incompressible Navier–Stokes equations," *J. Comput. Phys.* **59**, 308 (1985).
- <sup>34</sup>D. Yang and L. Shen, "Simulation of viscous flows with undulatory boundaries. Part I: Basic solver," *J. Comput. Phys.* **230**, 5488 (2011).
- <sup>35</sup>D. Yang and L. Shen, "Direct-simulation-based study of turbulent flow over various wavy boundaries," *J. Fluid Mech.* **650**, 131 (2010).
- <sup>36</sup>D. Yang and L. Shen, "Direct numerical simulations of scalar transport in turbulent flows over progressive surface waves," *J. Fluid Mech.* **819**, 58 (2017).
- <sup>37</sup>J. Komminaho, A. Lundbladh, and A. V. Johansson, "Very large structures in plane turbulent Couette flow," *J. Fluid Mech.* **320**, 259 (1996).
- <sup>38</sup>H. Kawamura, K. Ohsaka, H. Abe, and K. Yamamoto, "DNS of turbulent heat transfer in channel flow with low to medium-high Prandtl number fluid," *Int. J. Heat Fluid Flow* **19**, 482–491 (1998).
- <sup>39</sup>S. K. Robinson, "Coherent motions in the turbulent boundary layer," *Annu. Rev. Fluid Mech.* **23**, 601 (1991).
- <sup>40</sup>R. J. Adrian, "Hairpin vortex organization in wall turbulence," *Phys. Fluids* **19**, 041301 (2007).
- <sup>41</sup>J. Jeong and F. Hussain, "On the identification of a vortex," *J. Fluid Mech.* **285**, 69 (1995).
- <sup>42</sup>J. Zhou, R. J. Adrian, and S. Balachandar, "Autogeneration of near-wall vortical structures in channel flow," *Phys. Fluids* **8**, 288–290 (1996).
- <sup>43</sup>J. Zhou, R. J. Adrian, S. Balachandar, and T. M. Kendall, "Mechanisms for generating coherent packets of hairpin vortices in channel flow," *J. Fluid Mech.* **387**, 353 (1999).
- <sup>44</sup>R. J. Adrian, C. D. Meinhart, and C. D. Tomkins, "Vortex organization in the outer region of the turbulent boundary layer," *J. Fluid Mech.* **422**, 1–54 (2000).
- <sup>45</sup>E. G. Kastrinakis and H. Eckelmann, "Measurement of streamwise vorticity fluctuations in a turbulent channel flow," *J. Fluid Mech.* **137**, 165 (1983).
- <sup>46</sup>R. F. Blackwelder and R. E. Kaplan, "On the wall structure of the turbulent boundary layer," *J. Fluid Mech.* **76**, 89–112 (1976).
- <sup>47</sup>J. Kim, "On the structure of wall-bounded turbulent flows," *Phys. Fluids* **26**, 2088 (1983).
- <sup>48</sup>J. Kim and P. Moin, "The structure of the vorticity field in turbulent channel flow. Part 2. Study of ensemble-averaged fields," *J. Fluid Mech.* **162**, 339–363 (1986).
- <sup>49</sup>L. Shen and D. K. P. Yue, "Large-eddy simulation of free-surface turbulence," *J. Fluid Mech.* **440**, 75 (2001).
- <sup>50</sup>J. Jeong, F. Hussain, W. Schoppa, and J. Kim, "Coherent structures near the wall in a turbulent channel flow," *J. Fluid Mech.* **332**, 185–214 (1997).